



*Rice University, Department of Bioengineering*

*Master of Bioengineering – Applied Bioengineering*

Summer Research for Credit Final Report

Ibrahim Al-Akash

Sempionatto Lab for Biosensor R&D



#### Author's Note

I would like to express my sincere gratitude to Dr. Sempionatto for her continued support throughout this session and for giving me the privilege of working in her world-class laboratory.

## Table of Contents

Abstract.....	3
Summer Research for Credit Final Report .....	4
Biosensors Overview.....	5
PCB Project .....	9
PCB Design .....	10
PCB Fabrication .....	20
PCB Next Steps .....	26
Electrode Design Project .....	29
Electrode Design Criteria .....	30
Electrochemistry FEA Simulation Phase.....	35
Electrode Fabrication Phase .....	46
Electrode Study Next Steps .....	55
Concluding Remarks and Future Outlook.....	61
References .....	63

## Abstract

This report summarizes two independent research projects I undertook during the summer session in the Sempionatto Lab. My original assignment was to design, fabricate, and prototype a custom four-layer printed circuit board (PCB) that could serve as a modular platform for electrochemical biosensors across the lab's various applications. I completed the entire schematic and layout using KiCAD and generated the necessary fabrication files. However, due to long supplier lead times and delays in university procurement, I was unable to get the board ordered in time to complete fabrication and testing during the course.

With a few weeks remaining, I decided to pursue a new project based on an observation that caught my attention during lab shadowing – nearly all biosensor electrodes use the same circular geometry, yet no one I asked could point to a strong justification for it. That curiosity led me to propose a new study to investigate whether modifying the geometry of electrochemical electrodes, while keeping the amount of material constant, could improve performance. I designed a wide range of novel geometries, simulated them using finite element analysis (FEA) in COMSOL, and developed algorithms to evaluate each design using metrics I derived for power efficiency and charge symmetry. I then selected five top-performing designs and fabricated them using inkjet printing.

Although the PCB project remains in progress, this secondary project has already produced promising results and will continue into the fall semester with benchtop testing and experimental validation. Taken together, these projects reflect my initiative, technical versatility, and commitment to meaningful research that could inform future biosensor design in the Sempionatto Lab and beyond.

*Keywords:* PCB design, electrochemistry, biosensors, finite element analysis, inkjet printing

### Summer Research for Credit Final Report

Given my background in electronics, circuit design, and embedded systems, I was initially assigned by Dr. Sempionatto to lead the development of a general-purpose PCB for the lab. The goal was to create a modular, customizable interface for multiplexed electrochemical experiments to accelerate development across the diverse biosensor platforms being explored in the group.

The Sempionatto Lab is currently developing several cutting-edge biosensors targeting a range of health applications. These include a continuous, non-invasive hormone sensor for women's health that monitors luteinizing hormone (LH), follicle-stimulating hormone (FSH), estrogen, and human chorionic gonadotropin (hCG) in sweat; a breast cancer biosensor that monitors treatment effectiveness by correlating estrogen levels in interstitial fluid (ISF) to tannic acid concentrations; a transplant patient infection sensor that detects immune responses through inflammatory biomarkers; and a mental health biosensor that integrates EEG and pulse tracking with ISF-based analyte detection for cortisol, glucose, and lactate.

To build a robust and scalable electronics platform for these applications, I needed a strong understanding of the underlying electrochemical sensing mechanisms. This motivated a deeper exploration into how biosensors operate at a systems level from the redox reactions at the electrode surface to the analog signal conditioning and digital acquisition required for interpretation. By grounding the PCB development effort in the real-world needs of the lab's sensor portfolio, I sought to ensure that the resulting system would be not only technically sound, but also broadly applicable across current and future biosensor designs.

## Biosensors Overview

A biosensor is a device that integrates a biorecognition element with a transducer to convert a biochemical interaction into a measurable electrical signal [1]. A typical biosensor uses a three-electrode design to stimulate and read electrical signals, which includes a working electrode (WE), counter electrode (CE), and reference electrode (RE) as shown in Figure 1.

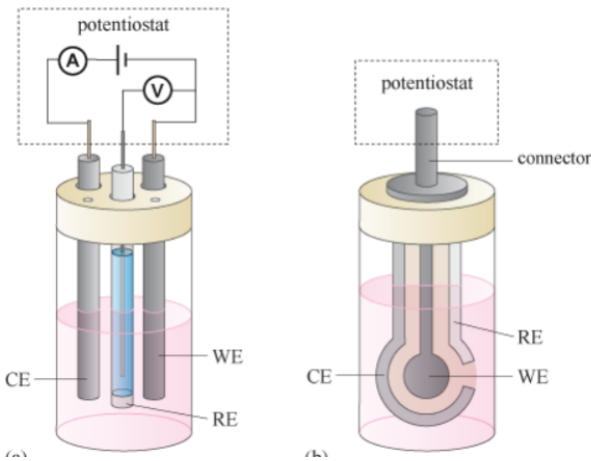
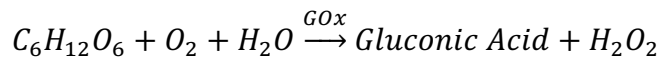
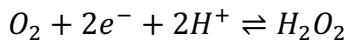


Figure 1. Typical three-electrode electrochemical cell configurations.

The WE is the site of the primary redox reaction and is where the target analyte undergoes either oxidation or reduction. The RE maintains a constant reference potential (typically pinned at 0 V), enabling accurate control of the potential at the WE. The CE completes the circuit by allowing current to flow and balancing the electron transfer at the WE. Both the WE and CE can be functionalized with biorecognition elements, such as enzymes or catalysts, to selectively interact with the target analyte. For example, in a glucose biosensor the glucose oxidase enzyme (GOx) is immobilized on the surface of the WE and CE and catalyzes the oxidation reaction with glucose forming gluconic acid and hydrogen peroxide:



Hydrogen peroxide then reduces the cathode resulting in a current flow:



$$i(t) = \frac{dQ}{dt} \propto e^{-}$$

Between the WE and CE a voltage is applied to deplete the oxygen and the current flowing through the electrode cell is measured which is relative to the direction of the oxygen concentration, as defined by the Cottrell equation:

$$i(t) = \frac{nFAC^{\frac{1}{2}}}{\left(\pi^{\frac{1}{2}}t^{\frac{1}{2}}\right)} \quad (1)$$

Where  $i(t)$  is current as a function of time,  $n$  is the number of electrons transferred,  $F$  is the Faraday constant,  $A$  is the electrode surface area, and  $C$  is the concentration of the analyte

Several electrochemical techniques are used to characterize biosensor performance including cyclic voltammetry (CV), chronoamperometry (CA), potentiometry, and electrochemical impedance spectroscopy (EIS). In CV, the voltage applied to the electrode is cycled continuously between a negative and positive potential and the current is measured producing a characteristic oxidation/reduction curve (Figure 2).

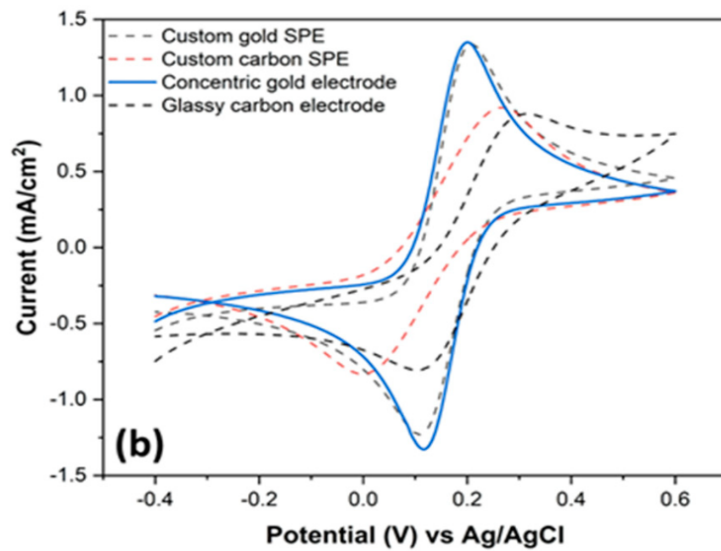


Figure 2. Sample CV measurement reading for various types of electrodes in a biosensor [2].

CA is a technique that fixes the voltage to a specified value, and tracks changes in current over time. This is used typically to create a stepwise response to sequential addition of a known concentration of analyte to the WE so the researcher can generate a calibration curve of analyte concentration vs. electrical current (Figure 3).

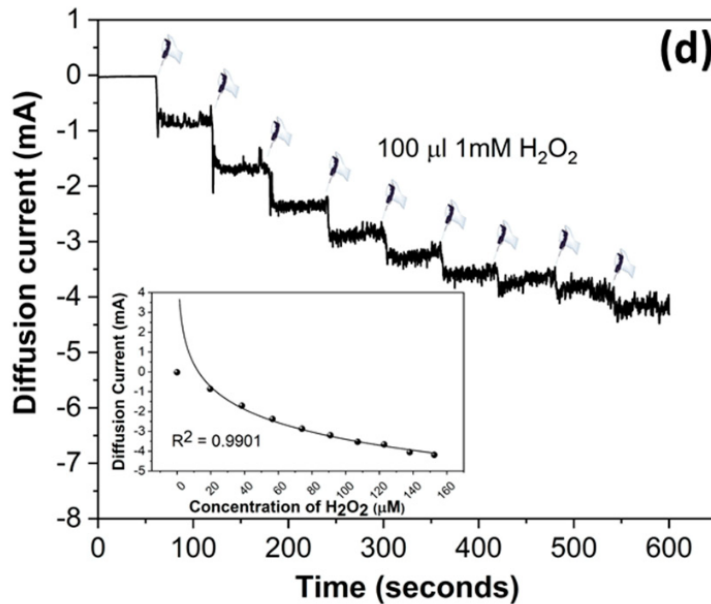


Figure 3. Sample CA measurement reading for a biosensor [2].

Potentiometry, typically performed in a two-electrode setup (WE and RE only), measures the potential difference between the WE and RE, governed by the Nernst equation:

$$E_{sample} = E_0 + \left( \frac{2.3RT}{nF} \right) \log a_{ion} \quad (2)$$

Where  $E_{sample}$  is the voltage or potential of the WE,  $E_0$  is the reference potential of the RE,  $R$  is the gas constant,  $T$  is the temperature at the electrode,  $n$  is the number of ions, and  $a_{ion}$  is the chemical activity of the ion

EIS is another technique that probes both resistive and capacitive elements of the electrode interface. By applying an AC voltage and measuring the resulting impedance, EIS can assess whether enzyme immobilization was successful and monitor interfacial binding events. A typical EIS result is presented in Figure 4.

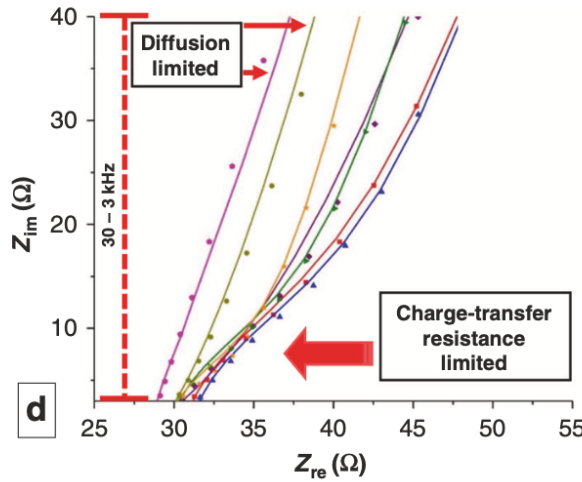


Figure 4. Sample EIS measurement for a biosensor [3].

In sweat-based sensors and other wearable biosensing platforms, microfluidics are often integrated to precisely control sample flow to the WE. This is particularly critical in ensuring reliable concentration measurements, especially under varying sweat rates. Impedance sensors are often included in these platforms to track fluid flow rate and volume in real-time.

## PCB Project

The development and testing of novel biosensors often rely heavily on access to multiple types of benchtop laboratory equipment—potentiostats, impedance analyzers, and iontophoresis stimulators—to evaluate electrochemical performance. However, this approach presents several challenges. It is resource-intensive, time-consuming, and not scalable, particularly when testing a wide variety of sensor configurations or conducting repeated trials. Additionally, many wearable biosensors especially those based on sweat analysis require auxiliary stimulation systems such as iontophoresis, which further complicates the experimental setup and increases equipment demands. This is where my role began. I was tasked with designing a general-purpose PCB capable of performing a wide array of electrochemical measurements, including CV, CA, potentiometry, and impedance measurement, as well as delivering low-current stimulation for iontophoresis. The design also needed to interface with various biosensor platforms through a modular architecture. The resulting PCB is intended to serve as an all-in-one measurement platform that enables plug-and-play compatibility with electrochemical sensors under development in the Sempionatto Lab. This eliminates the need for complex wired setups involving alligator clips or taped connections, which are often a source of signal noise and measurement inconsistency. By relying instead on robust PCB-mounted connectors and embedded copper traces, the system enhances both electrical reliability and experimental reproducibility. In addition to improving data quality and reducing the burden on researchers, this PCB design strategy future-proofs the lab's workflows. Its modular nature and comprehensive functionality ensure compatibility with future biosensor innovations, supporting the lab's long-term vision of creating integrated, compact, and field-deployable diagnostic platforms. This design not only supports current research efforts but also lays the foundation for

scaling up toward real-world applications in point-of-care diagnostics and personalized health monitoring.

### **PCB Design**

The PCB was successfully designed with all key functionalities required for advanced biosensor testing, including electrochemical signal processing, wireless communication, and compact power management. The architecture integrates elements inspired by two reference designs: one for a solar-powered electrochemical sensor frontend [4], and another for a multiplexed biosensor platform that informed the microcontroller selection and programming methodology [5]. The development process began with identifying and organizing the components for the electrochemistry frontend, guided by a reference block diagram from the solar-powered wearable flexible biosensor research paper (Figure 5). Based on this, a full bill of materials (BOM) was compiled, taking into account component availability, datasheet-recommended footprints, and integration constraints.

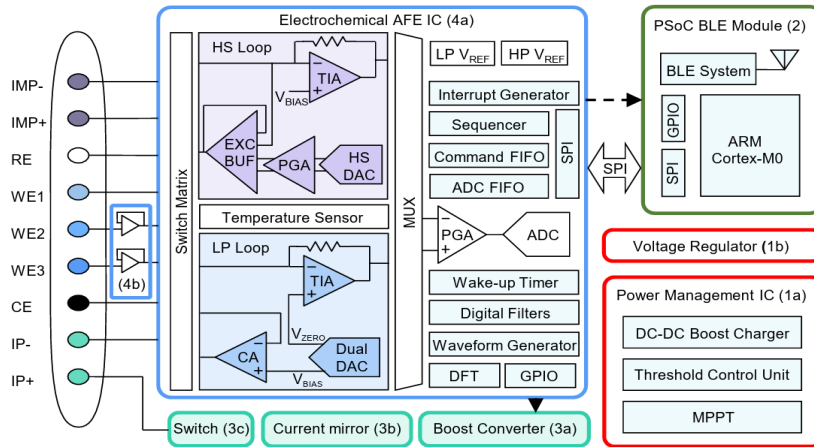
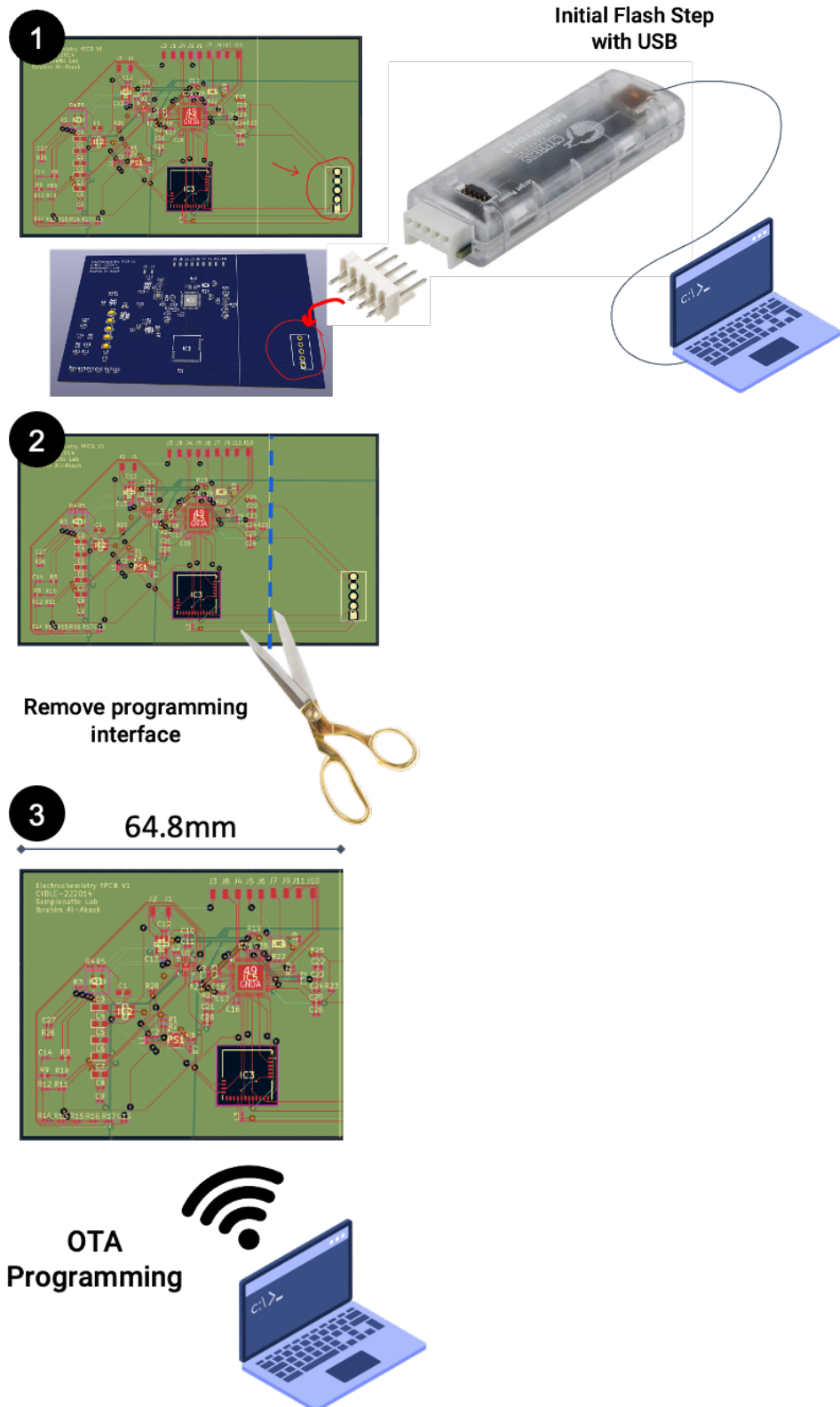


Figure 5. Block diagram of electrochemistry frontend circuit.

Using KiCAD, I created a full schematic incorporating the analog frontend, power supply, and microcontroller units. In schematic design, logical connections are defined between components, laying the groundwork for physical PCB layout. A key challenge in this project was

working with the PSoC (Programmable System-on-Chip) microcontroller platform, which was unfamiliar at the outset. Its development environment, programming tools, and hardware configuration were non-trivial to set up. However, through research and review of unrelated journal papers, I discovered an innovative solution to streamline programming. Instead of relying on permanent debug headers (which would increase the PCB footprint) a sacrificial programming region was added to the board. This region connects the necessary PSoC programming pins to a MiniProg3-compatible header. Once programmed, the sacrificial tab can be physically removed to minimize the board's size, and future updates can be pushed wirelessly via over-the-air (OTA) programming (Figure 6 and Figure 7).



*Figure 6. Programming interface connection procedure. 1) Header pins are soldered to programming pins and programmed via MiniProg 3 programmer with computer. 2) Once programming is completed, the sacrificial region of the PCB is cut off making the PCB much more compact. 3) Any additional software updates can be sent to the board via OTA programming.*

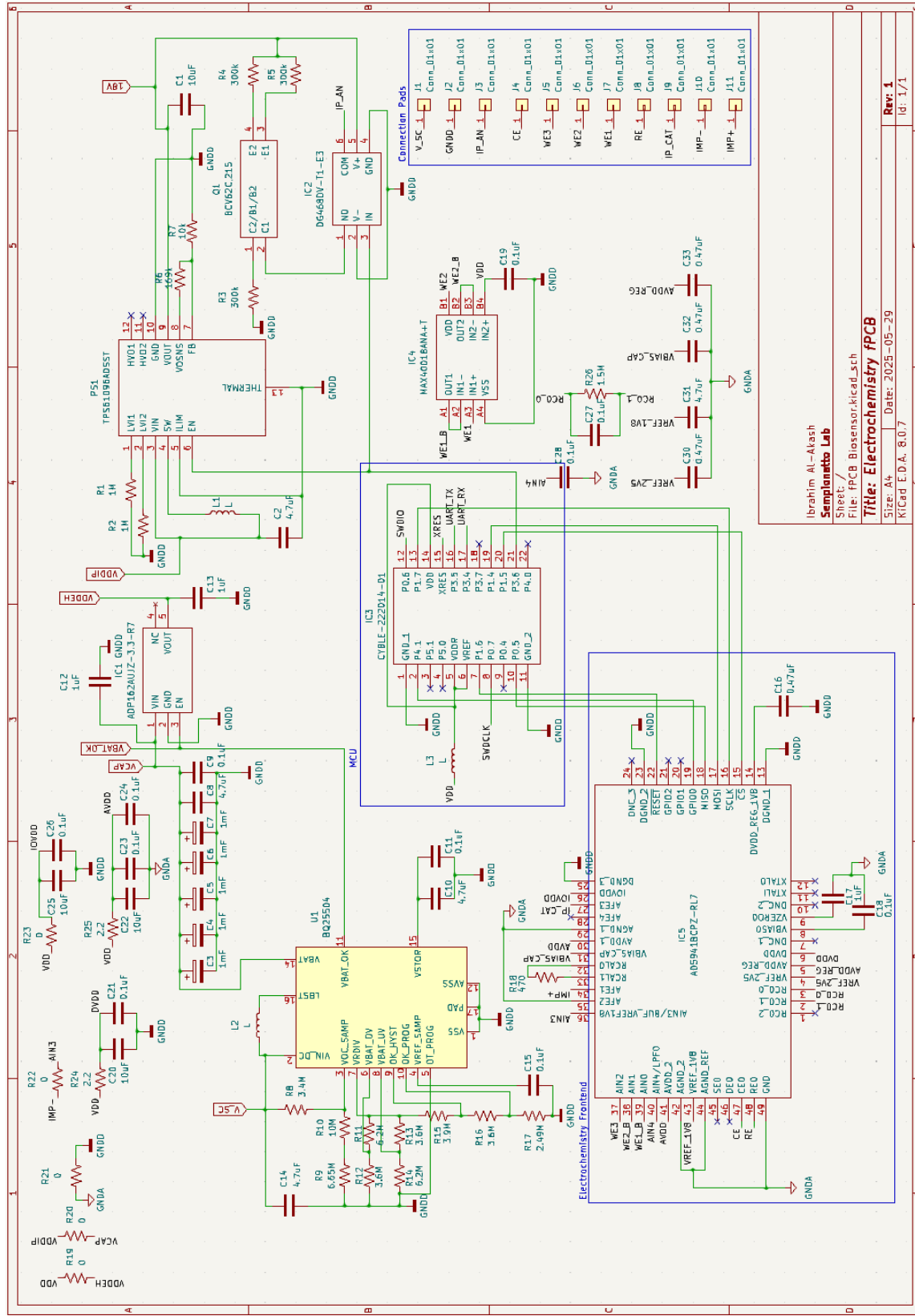


*Figure 7.* Schematic for custom PCB design.

After completing the schematic, I developed the physical PCB layout (Figure 8-Figure 12). This process involved placing components and routing traces across a 4-layer board stack-up, with signal-ground-power-signal layer ordering. Given the sensitivity of analog electrochemical measurements, special attention was paid to signal integrity, noise reduction, and manufacturability. Design considerations included:

### **Electrical Performance**

- Separated analog and digital domains to reduce coupling and noise
- Routed high-speed signals orthogonally to low-speed signals to minimize crosstalk
- Kept analog traces sufficiently spaced to reduce mutual inductance and parasitic capacitance
- Placed bypass and decoupling capacitors as close as possible to the power pins of ICs
- Impedance-matched high-speed signals (such as UART lines) through appropriate trace width and spacing
- Sized traces based on expected maximum current using IPC standards
- Positioned analog ICs close to critical signal sources to minimize trace lengths and noise pickup

### **Design for Manufacturing (DFM) and Design for Testing (DFT)**

- Selected component sizes that balance compactness with hand-assembly feasibility
- Enlarged key passives expected to require debugging to allow easier soldering/rework
- Minimized through-hole components to streamline assembly
- Ensured all connectors matched the mechanical specs of their mating parts
- Added test points to key signal traces for validation with lab equipment

## Mechanical and Layout Standards

- Followed manufacturer DFM rules and cleared all warnings
- Used a 4-layer stack-up (Signal, Ground, Power, Signal) to improve noise isolation
- Chose generous trace/space tolerances within the PCB fab's capabilities to lower cost
- Kept the Bluetooth antenna region free of copper pours and signal traces to avoid detuning or interference
- Verified all layout recommendations for ICs per their datasheets
- Optimized silkscreen readability to aid assembly and debugging

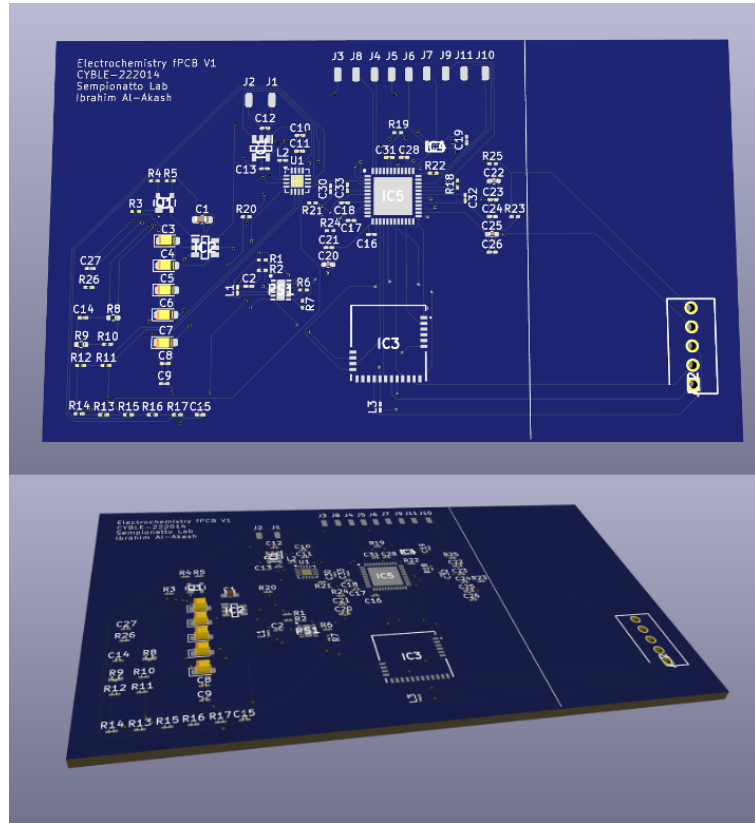


Figure 8. 3D rendering of PCB layout.

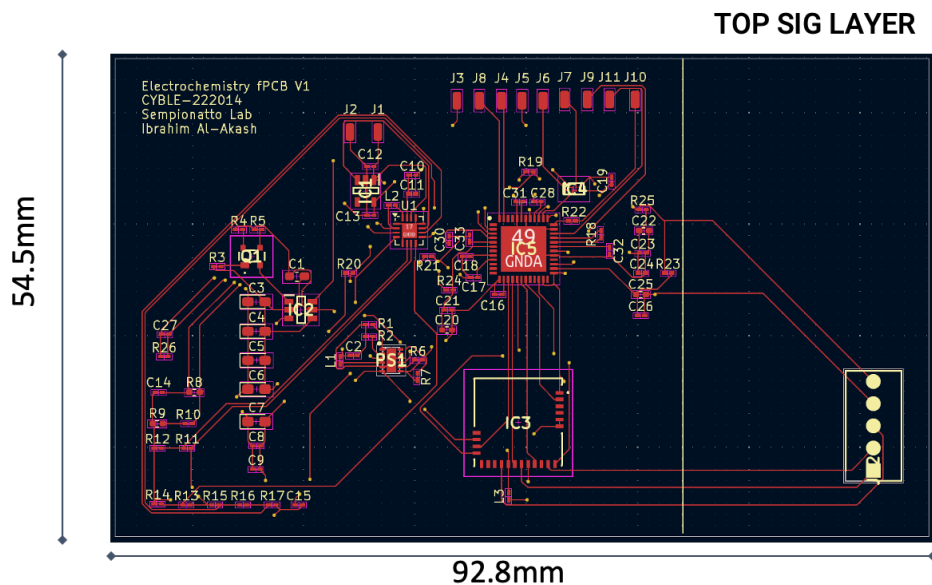


Figure 9. Top signal layer in PCB layout with board dimensions. Red indicates copper traces and solder masks, and yellow indicates silkscreen.

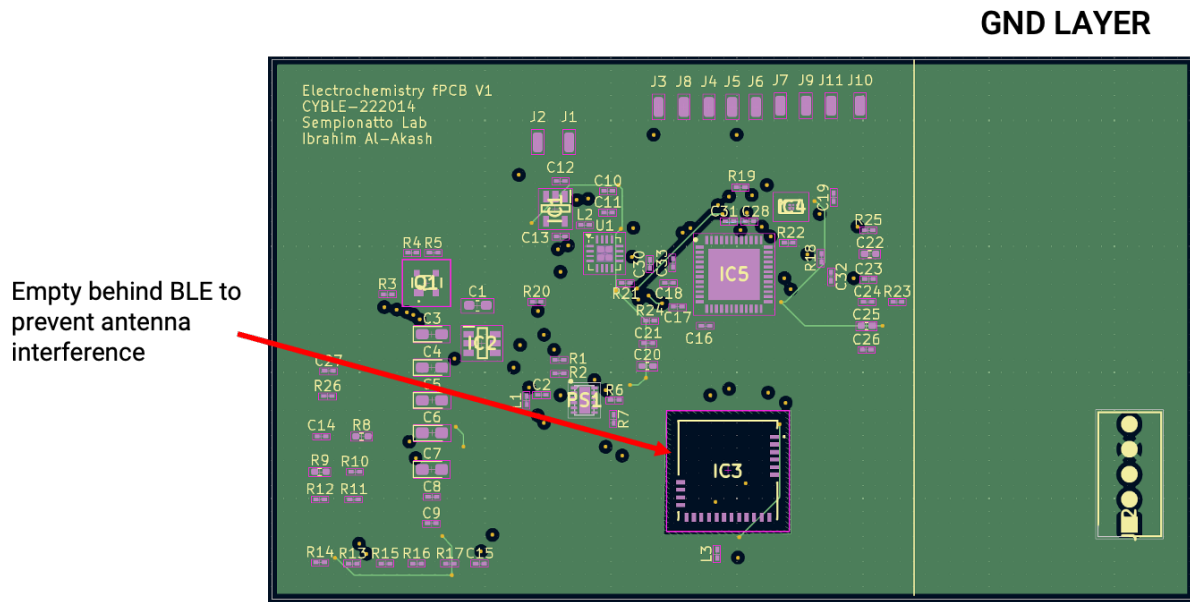


Figure 10. Ground layer in PCB layout. Green indicates copper pour.

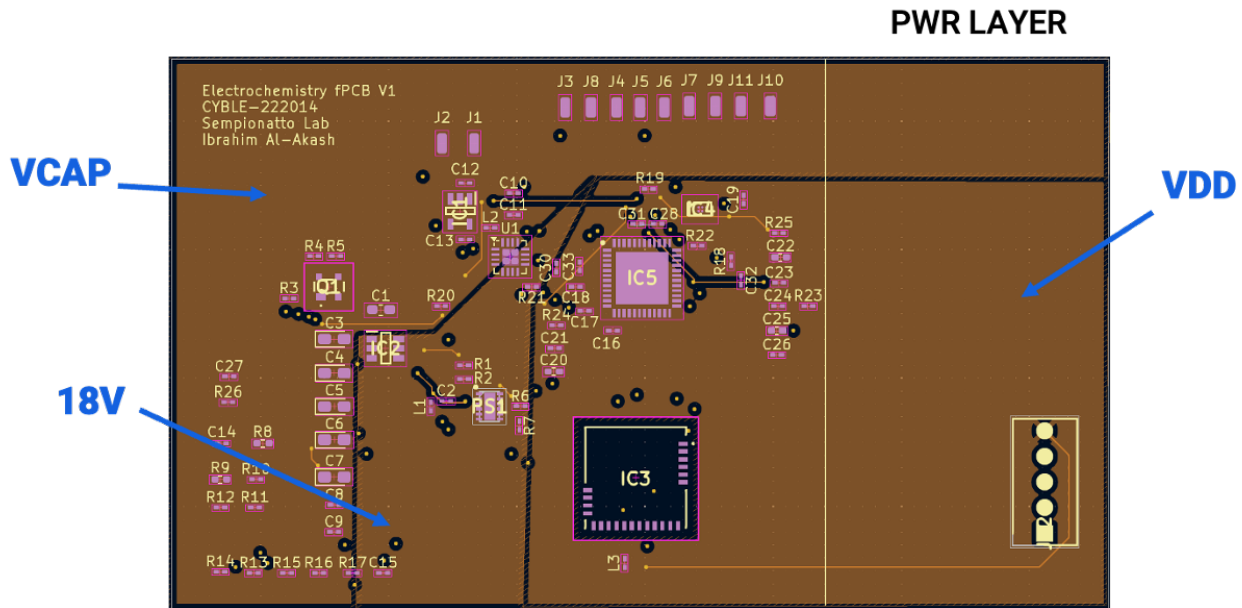


Figure 11. Power layer in PCB layout. Orange indicates copper pour.

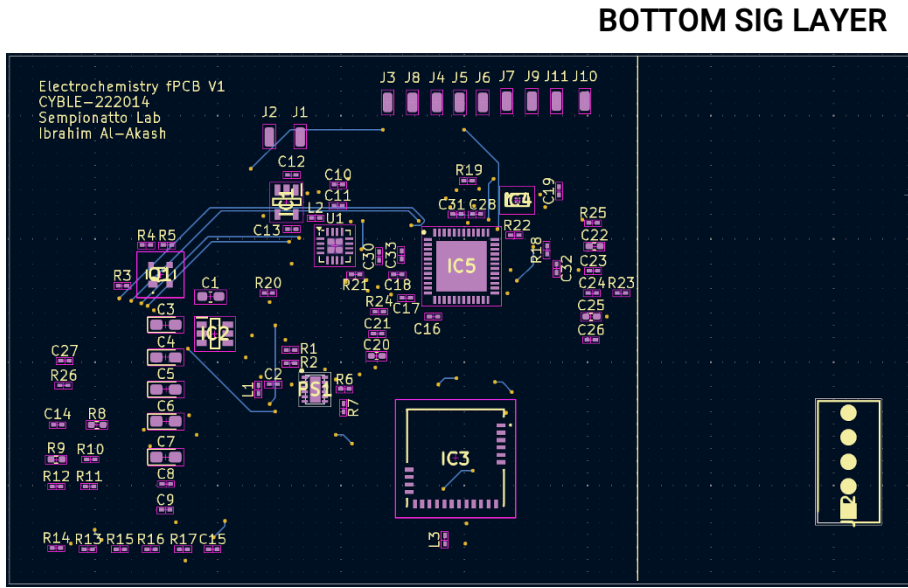


Figure 12. Bottom signal layer in PCB layout. Blue indicates copper traces.

The final layout includes a dedicated battery interface using solder pad terminals (Figure 13), and modular connector regions to interface with any biosensors incorporating the standardized connector design (Figure 14). This modular architecture supports the long-term goal of creating a general-purpose biosensing platform for rapid sensor characterization. While awaiting PCB fabrication, evaluation boards for the analog frontend and PSoC microcontroller were ordered to allow firmware development in parallel. Once the PCB arrives, the firmware will be ported to the custom hardware, and initial testing can begin using both commercial and custom-fabricated biosensors.

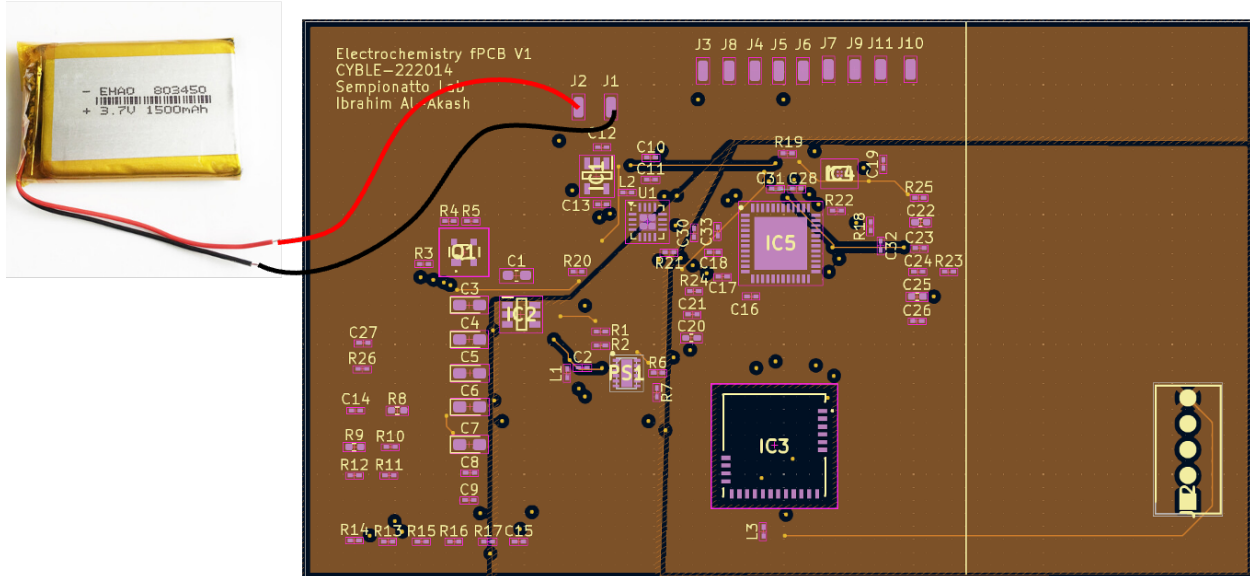


Figure 13. Battery connected to solder pads.

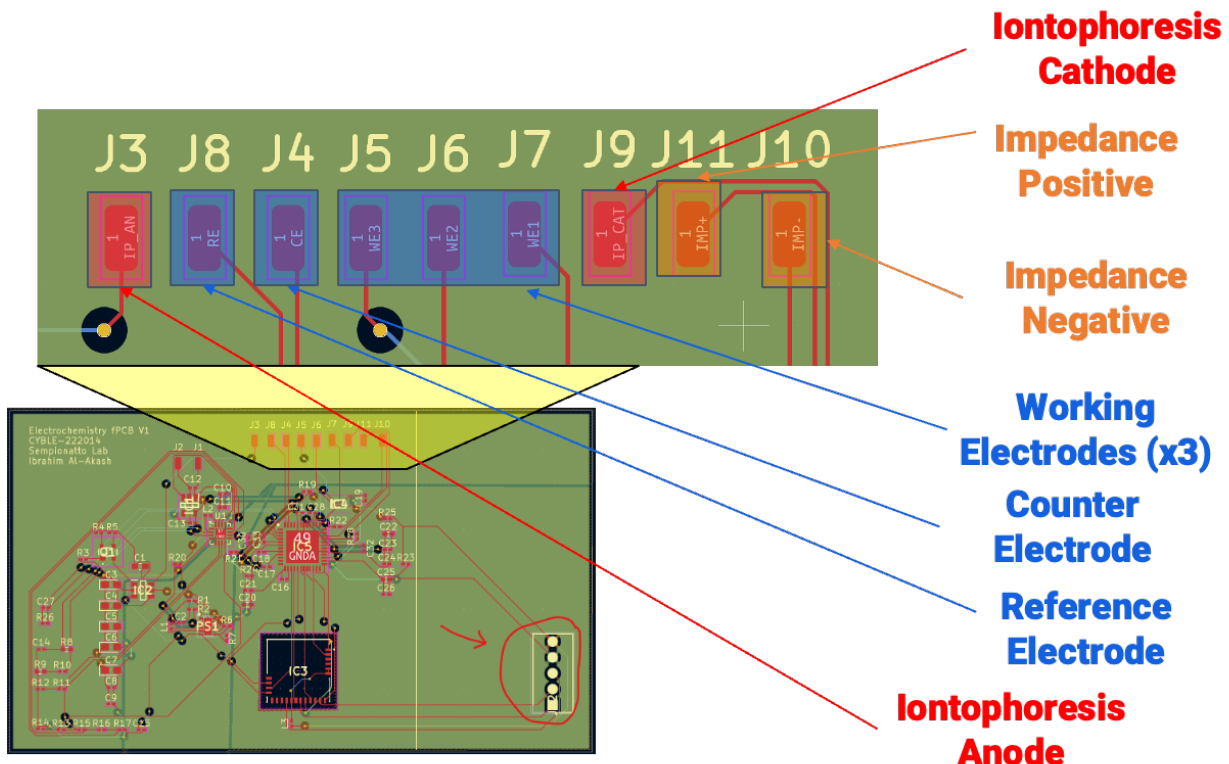


Figure 14. Modular solder tab design.

### ***PCB Fabrication***

To fabricate the PCB, I initially planned to follow the same approach I used for my senior design project: sending the Gerber files to a fabrication service such as JLCPCB. This is typically a straightforward process, and I designed the board to use only surface-mounted components so that assembly could be completed quickly in 10-15 minutes with a reflow oven. However, Dr. Sempionatto had recently acquired an LPKF U4 Protolaser, and she preferred that we attempt in-house fabrication. The first step was to evaluate whether the machine specifications could meet the design requirements. The LPKF U4 supports up to six-layer fabrication, which was compatible with the four-layer stack-up designed in KiCAD. However, because the lab was interested in developing a flexible PCB (fPCB), sourcing a compatible substrate became a critical bottleneck. The Protolaser included a small sample sheet of flexible copper-clad laminate material for demonstrations, but no documentation or manufacturer details were available for ordering more of the material. Attempts to identify the material through LPKF's website were unsuccessful, prompting direct outreach to LPKF support. I contacted LPKF customer support by email, but the response time was slow. I followed up with a phone call, but neither channel provided useful guidance. In both cases, I was advised to Google the material myself, which was an unacceptable and dismissive response given that I had already conducted thorough searches and was unable to find the information (Figure 15).

**Support Group** <support.usa@lpkf.com>  
to Support, me ▾

Ibrahim Al-Akash  
We don't have the same material in the US as they do in Germany. I can suggest to search out board company's to find the nearest solution.

Tim Blake  
Field service  
LPKF Laser & Electronics - North America  
12555 SW Leveton Drive, Tualatin, OR 97062  
Phone: +503.454.4229  
Fax: 503.682.7151

**Ibrahim Al-Akash** <isa1@rice.edu>  
to Support ▾

Hi Tim,

Thanks for the update.

Could you please send me the names of any board companies you recommend where I might be able to find a similar material here in the US?

Best regards,  
Ibrahim Al-Akash  
Rice University, Department of Bioengineering  
Sempionatto Lab

**Support Group**  
to me, Support ▾

The best bet would be to describe the material in google search to see what companies come up.

Figure 15. Initial response from LPKF customer support.

Only until I sent a complaint to their main headquarters in Germany did I receive a proper response explaining the material they use is a polyimide copper-clad laminate material and that they don't sell the material themselves, so we need to source it either from Dupont, EBay, or a Chinese manufacturer (Figure 16 and Figure 17). This introduced a new logistical challenge. Among the suggested suppliers, only eBay carried the double-sided version of the substrate needed for a four-layer PCB. Unfortunately, the university's procurement platform (Quartz) does not allow purchases from eBay, and the other listed vendors only offered single-sided copper-clad substrates. While I was waiting for the responses from the LPKF support team, I did more research on the fabrication process with their machine. I learned how to make a 4-layer PCB from base material to finished board, but unfortunately the Protolaser alone is insufficient

and we would need additional equipment amounting to over \$50,000 to be able to fabricate the board in-house.

Ibrahim Al-Akash <isa1@rice.edu>  
to info ▾

Thu, Jul 10, 12:43 AM ⚡ ← ⋮

Dear LPKF Team,

I am writing to formally submit a complaint regarding the unprofessional and dismissive treatment I received from your North American support team, both via email and over the phone.

On July 9th, I emailed Tim Blake from your support team to inquire about materials used in the LPKF Protolaser demo. Instead of receiving technical assistance or a recommendation, I was told to "describe the material in Google search to see what companies come up." This was not only unhelpful but conveyed a clear lack of interest in supporting my legitimate customer request.

To make matters worse, when I followed up with a phone call to your support line, the representative I spoke to was rude and displayed a noticeably poor attitude. Rather than helping clarify the materials or offering any useful direction, the conversation was dismissive and disrespectful.

This level of service falls far below the standards I would expect from a company like LPKF, particularly given the technical nature and price point of your equipment. As a researcher at Rice University using your tools in an academic research setting, I rely on dependable and knowledgeable support. So far, the experience has been the worst I've encountered from any equipment provider.

I request that this issue be escalated and that someone with proper technical expertise follow up with me directly regarding my original inquiry.

Sincerely,  
Ibrahim Al-Akash  
Rice University, Department of Bioengineering  
Sempionatto Lab

*Figure 16.* Complaint email I sent to LPKF HQ.

Hi Ibrahim Al-Akash,

I was informed today of your escalation and want to thank you for bringing your concerns to our attention. I'm sorry the experience felt frustrating—it's clear we could have been more attentive to your needs and communicated more effectively along the way.

While we didn't have an immediate answer to your question at the time, we recognize the importance of staying engaged and ensuring you feel supported throughout the process. That's an area we're actively working to improve.

We are currently seeking the answer and have sent an inquiry to the calibration team to find out what that exact material is. As that particular piece of material is not specified anywhere and is used for the calibration and simply left there as a reference, we don't have the information on hand.

We appreciate your patience and understanding. Below is a list of companies and contacts that would have the materials to meet your needs. I have also copied our sales director as we want to make sure we are all learning from this experience.

Below is our list of contacts to source flex PCB Polyimide and PET/Mylar materials, various laminated RF/MW materials, Thin Film metallization, Direct Bond Copper (DBC) or Thick Film metallization on Alumina/fired ceramics, as well as fired or unfired LTCC and LTCC Carbon Tape materials for ProtoLaser operations.

We do carry standard FR4 materials here in Oregon.

- Nearly any laminated RF substrates from Rogers Corporation, Taconic, Panasonic and FR4 can be processed with the LPKF patented laser hatch & delamination feature on the ProtoLaser H4, S4, U4 and R4 systems allowing rapid Cu/metal removal. Please see attached for application comparison details and general substrates guide.
- DuPont Pyralux TK, TFH and AG flex materials can also be processed with hatch & delamination and materials can be sourced through Insulectro. Datex Instruments also provides flex polyimide substrates that can be processed with the ProtoLaser S4, U4 and R4 models with hatch & delamination removal or by direct laser ablation with the ProtoLaser U4 or R4; ablation removal is dependent on the material and metallization thickness.
- Thin film Cu/Ni/Au fired ceramics (Al<sub>2</sub>O<sub>3</sub>, AlN) or green/unfired ceramics can be sourced through Rogers Curamik, Steller Industries, Compex Corp or DuPont - Microcircuit Materials which are all listed below. They each have contacts or a vendor which would apply thin film, thick film or DBC copper to their materials and may offer TiW, TaN, W/Ni, W/Ni/Au metallization, etc. Specific metallization and materials can be requested based on the customer needs.

Hi Ibrahim,

I hope you are doing well and wanted to provide some additional details on the test sample included with the ProtoLaser systems and material options available for processing.

I confirmed with our global headquarters in Germany on the test materials provided with each ProtoLaser after final system testing and details can be found below.

A 1.5mm sheet of FR4 is provided with the calibration samples on the ProtoLaser S4 and U4 models; this is available as SET-10-1118N through our global headquarters in Germany.

With the ProtoLaser R4 picosecond laser system, a thin sheet of 8 mil (200um) 104 ML material is provided; part number 119571:

SET-10-1118N	Base Plate FR4, 229 mm x 305 mm (9"x12"), 00/18 µm copper plated, 1.5 mm thickness, predrilled with 3 mm registration holes,	
10 pieces	\$143.75	(1 sheet is included with ProtoLaser S4/U4 with the system test sample)
- Made in China -		
119571	Thin Laminate 104 ML 5/0 µm 305 (k) x 229 x 0.2 mm (9" x 12") with protection foil 8 mil thick Single Sided thin laminate material for outer layers, ½ oz. Cu Includes peel off protective foil. Qty 1 \$121.00	(included with ProtoLaser R4)

As our North America office here in Oregon sources FR4 material here in the U.S., we do not stock SET-10-1118N but this can be purchased if needed. The FR4 material options we offer are detailed in the attached Tools & Materials pricelist with single and double sided FR4 found on page eight (8) and the multilayer kits and single sheet options on page 10.

*Figure 17.* LPKF subsequent response that provided the information I had originally requested.

To better understand the PCB fabrication process, the stack up for the PCB and how the materials are configured in a 4-layer PCB is outlined in Figure 18.

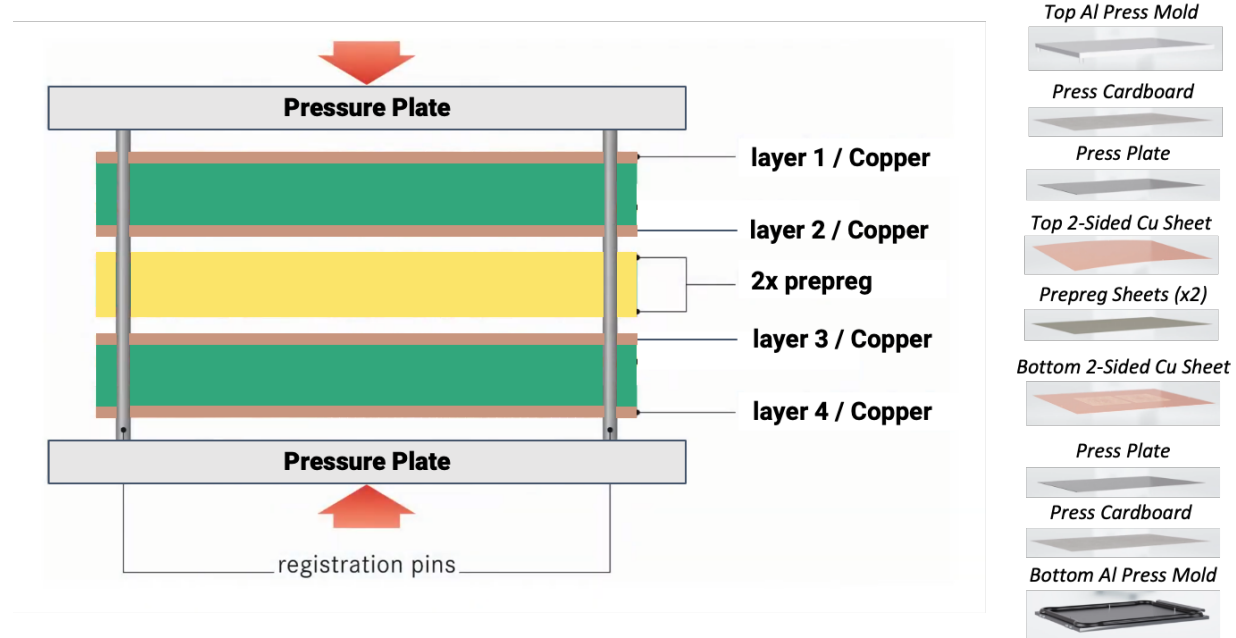


Figure 18. PCB layering scheme for my 4-layer board.

In total, I found the entire fabrication process takes 9 steps (Figure 19). These steps require additional equipment including the LPKF MultiPress S, LPKF Contac S4, LPKF UV Exposure machine, and a UV inkjet printer. First, the inner copper layers of the board are laser cut in a subtractive manufacturing process with the Protolaser. The inner layers need to be cut first because in the next step when the layers are pressed together, the inner layers will no longer be accessible. Next, the layers are aligned precisely in an aluminum press mold according to the stack up and pressed together into a thin sheet board with the MultiPress in the lamination step. The laminated assembly is then placed into the Protolaser and the vias and mounting holes are drilled through. Then, the vias need to electrically connect the layers together, which is done with the Contac machine via an electroplating process to deposit copper on the inside of the vias. Next, the outer copper layers (the top and bottom in this case) are laser cut with the Protolaser. Now technically the board has the functional circuit. However, for assembling the chips and passive components additional steps are required. First, a UV-curable resin is painted onto the

board. Then, a laser cutter burns a design into a transparent film substrate which will serve as the UV mask. The substrate is then aligned on the board precisely to cover all the copper surfaces that need to be exposed for soldering including all solder pads and through-hole vias. The LPKF UV Exposure machine then cures the resin in all the exposed regions, and the uncured resin is washed away leaving the solder pads exposed while insulating the traces and other conductive elements. This prevents shorting between solder pads and traces making soldering much easier. With this finished surface, the board can be reflow soldered in a reflow oven which takes only 10-15 minutes as opposed to hand-soldering all the components which can take many hours. However, without any of the pads labeled there is no way to tell where to place each component during the assembly process. This is where the final step comes in: silkscreen printing. The silkscreen is a layer that is printed on the board enabling the user to identify where each component goes and in what orientation polarized components need to be placed. This final step requires a UV inkjet printer to precisely print the silkscreen since the labels are very small to fit on the board and prevent overlapping with other silkscreens or the solder pads.



Figure 19. In-house PCB fabrication procedure.

Given these constraints, I pivoted back to the original plan of ordering from JLCPCB. However, I encountered new obstacles. JLCPCB requires Gerber files to generate an invoice for fabrication, but Quartzy does not allow file uploads or support JLCPCB as a vendor. To resolve this, I coordinated with multiple lab members and university staff to identify a workaround. I also showed Dr. Sempionatto the process I had used previously to order my senior design PCB. She contacted JLCPCB customer support and successfully obtained a formal invoice for the board, which I uploaded to Quartzy. Despite this, I encountered further delays. Several days passed before I received a response from the university procurement office, stating that they were unable to process the invoice, but providing no clarification. I followed up to request more information but received no further updates for over a week. By that point, it was clear the board would not arrive before the end of the summer session. Rather than lose this time, I immersed myself in various lab activities attending trainings and shadowing my lab mates to learn techniques such as distillation, screen printing, inkjet printing, biosensor functionalization, and performing cyclic voltammetry and chronoamperometry. This experience proved invaluable and ultimately sparked the idea for a second research direction: a geometry optimization study for inkjet-printed biosensor electrodes. This new project is detailed in the following sections.

### ***PCB Next Steps***

The next phase of the PCB development process will build on the lessons learned during the initial design and testing of the prototype board. Several key improvements are planned to enhance circuit reliability, optimize power management, and ensure better integration with the electrodes produced by the graduate researchers in-house and biosensor testing protocols.

First, the power management circuitry will be redesigned from scratch. The original design was based on the circuit topology adapted from the solar-powered electrochemical

sensing paper, which proved cumbersome to modify for the intended use case in this project.

Now that I have gained additional experience designing power delivery systems through my work on DialySafe at the Rice Nexus, it is clear that building a new circuit tailored to my system requirements will be more efficient and result in better performance. This new design will include cleaner regulation of analog and digital rails, better protection against startup transients, and a layout optimized for low-noise operation.

In parallel, the PCB layout itself will be updated to include copper ground pours on both the top and bottom signal layers, with stitching vias placed throughout the board to ensure robust grounding and minimal EMI susceptibility. This was not implemented in the original version because I was not yet aware of the importance of stitching vias in minimizing ground loop area and improving signal integrity. Having since studied this best practice through the DialySafe hardware project, I now plan to apply it here.

Additionally, signal visibility and debug capability will be improved by adding test points at critical locations in the analog front-end and power rails. This will allow for easier probing during initial bring-up and facilitate faster troubleshooting if the board does not function as expected. Connector design will also be revised: the current solder tab configuration for the sensor interface will be replaced with an FPC-compatible footprint to support standardized, secure, and reusable connections with the inkjet-printed electrodes. This will also reduce the risk of mechanical stress damaging the pads during handling and testing.

Once these updates are finalized in the design files, the revised PCB will be ordered through JLCPCB for fabrication. While awaiting board delivery, firmware development will begin using the evaluation boards (EVAL kits) for both the electrochemistry analog frontend IC and the selected MCU. By using the EVAL boards to validate the firmware logic and peripheral

configuration ahead of time, I can ensure a smoother transition when the custom PCB arrives.

Once the firmware is verified, the same codebase will be ported to the custom board with only minimal hardware abstraction changes.

After uploading the firmware onto the assembled PCB, I will begin a battery of electrochemical experiments using commercial sensors to validate system performance. These tests will include generating CV, CA, potentiometry, and impedance curves. I will also verify iontophoresis functionality by applying controlled currents through the current drivers and measuring the resulting current output and potential changes. If any issues are encountered during these tests, the circuit will be iteratively debugged and updated until it performs as expected.

Finally, once the full system has been validated and performance is consistent across multiple test cycles, the PCB layout will be refined for size and manufacturability. The initial version will use a rigid PCB form factor to simplify assembly, inspection, and measurement, but once the system is fully prototyped, it will be transitioned to an fPCB format. This final version will meet the form factor and flexibility requirements needed for integration into a wearable or patch-based biosensing platform, aligning with Dr. Sempionatto's vision for future applications.

### **Electrode Design Project**

When I was observing one of the other students printing an electrode design on the inkjet printer, I noticed there was an odd notch for the RE, and the CE didn't fully encircle the WE due to the notch. Curious, I asked how they decided what arc length to use for the CE vs. the RE and they stated they were simply following the designs that were done previously as convention. That response sparked a deeper curiosity—why this geometry? Was it truly optimal, or just inherited tradition? Coming from an engineering background, I wondered if the conventional design was the optimal use of material or whether there are better alternatives to enhance performance given the same amount of starting material or attain comparable performance with less starting material simply by changing the geometry. If efficiency can be significantly improved, then on a large scale this can potentially save manufacturers millions of dollars. Motivated by that question, I began researching electrode design strategies. To my surprise, I found that relatively few studies have focused specifically on electrode geometry as a tunable design parameter in biosensor optimization. Most biosensor research centers around improving the biorecognition layer, extending device lifetime, enhancing biocompatibility, or innovating around materials and power systems. Electrode geometry, despite being central to electrochemical performance, remained largely overlooked.

This gap in the literature inspired me to propose a novel research direction: a high-throughput electrode geometry optimization study. My hypothesis was that bio-inspired geometries could offer improved performance due to their natural evolution toward efficient transport and distribution. Such structures have already shown success in adjacent fields like soft robotics and biomimetic materials [6, 7, 8, 9]. I proposed a comprehensive end-to-end pipeline for this study, including custom electrode design, simulation using FEA, inkjet printing

fabrication, and bench-top experimental validation (Figure 20). Dr. Sempionatto reviewed and approved the project, allowing me to move forward. The goal was to systematically evaluate how varying electrode geometries affect electrochemical performance metrics such as current density, signal symmetry, power dissipation, and overall sensing efficiency.

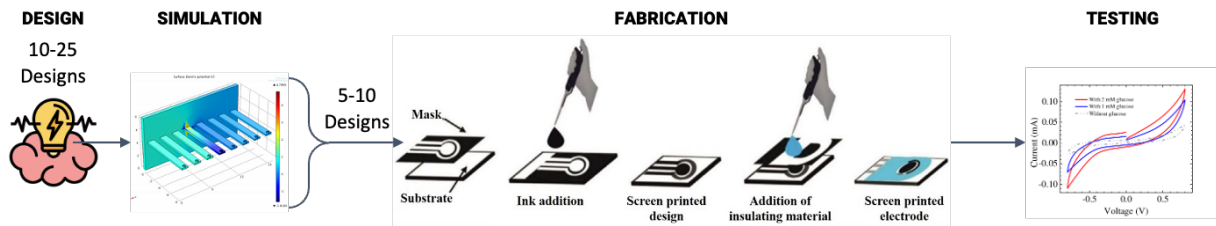


Figure 20. Electrode design study workflow pipeline.

Electrode geometry represents a highly leveraged but underexplored design space. Even subtle changes to shape and orientation can significantly impact field uniformity, current distribution, and signal stability especially in miniaturized or flexible biosensors. Optimizing this dimension could lead to meaningful advances in sensor reliability and efficiency, making it a promising new direction for research in the Sempionatto Lab and beyond.

### ***Electrode Design Criteria***

To isolate geometry as the sole independent variable influencing sensor performance, I established a set of design constraints to control for confounding factors across all electrode designs:

- The same materials would be used for the CE, WE, RE, traces, and connector pads. The CE and WE sensing regions would be made of carbon/Prussian Blue (PB) and the RE, traces, and connector pads would be made of silver/silver chloride
- Each design maintained a constant planar surface area of  $15 \text{ mm}^2$  for the carbon material and  $30 \text{ mm}^2$  for the silver/silver chloride material

- All designs used a uniform layer height of 65  $\mu\text{m}$ , representative of the expected inkjet print thickness with the available lab equipment
- The fabrication process was standardized across all designs using the same inkjet printer, ink formulations, and polyimide 3-mil Kapton substrate
- Electrodes were left unfunctionalized, and only direct  $\text{H}_2\text{O}_2$  detection will be tested, eliminating variability from enzyme kinetics and focusing purely on electrochemical performance
- Connector pad geometry and trace lengths were standardized across all designs to ensure consistent electrical interfacing with the CHI potentiostat and reduce experimental variability caused by differing contact quality

These constraints ensured a level playing field for design comparison. They also aligned with electrochemical design best practices such as maintaining a CE area greater than the WE to prevent current limitation, minimizing ohmic drop by placing the RE close to the WE, and avoiding capacitive coupling by keeping the CE at an appropriate distance from the WE. Additionally, achieving symmetrical current distribution at the WE surface was prioritized, as nonuniform current density can distort reaction kinetics, lead to uneven degradation, and impair measurement accuracy. Designs were also evaluated for their ability to minimize power dissipation and Joule heating, both of which can elevate noise, alter analyte behavior, or degrade sensor performance over time.

To provide performance baselines, I included a set of standard geometries adopted from published literature. From there, I designed a series of novel and bio-inspired geometries based on analogies observed in natural electrochemical systems. In biology, many systems involve a transduction site akin to the WE, a stabilizing comparator like the RE, and a return pathway like

the CE. These functional analogs appear in sensory networks, vascular branching, neural circuitry, and electroreceptive organs across species. I was particularly inspired by marine organisms and plant structures, where the evolutionary pressure for efficiency has produced geometries that may offer electrochemical advantages. In total, I sketched more than 25 electrode concepts by hand (Figure 21). Designs #1–10 were based on previous papers, #11–18 were original but not bio-inspired, and the remaining geometries drew from biological systems.

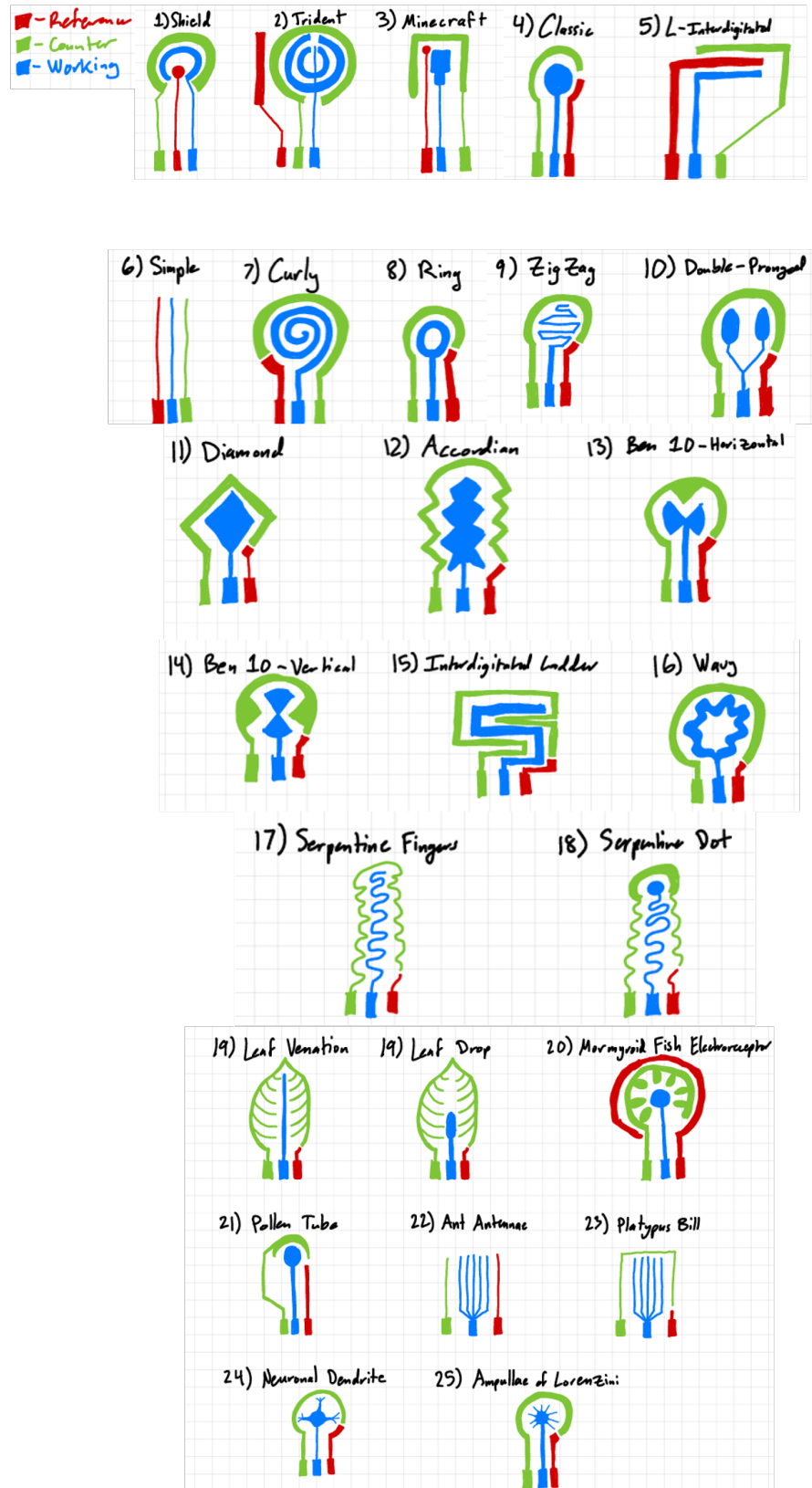


Figure 21. Hand sketched electrode design geometries. #1-10 are designs adopted from previous papers, #11-18 are novel designs which are not bio-inspired, and the remaining designs are bio-inspired.

To expand on a few of the bio-inspired examples:

- Leaf Venation and Leaf Drop designs: These designs mimic the capillary branching in leaves, aiming to promote even current distribution akin to how leaves distribute water [10]. This could result in more uniform sensing activity and lower spatial signal variance
- Mormyrid Fish design: Inspired by mormyromasts, which are specialized electroreceptors in certain fish, this geometry distributes WE and CE radially around a central RE to simulate spherical field detection and improve signal integration from weak inputs [11]
- Pollen Tube design: This plant structure exhibits electrotropism, responding to electrical cues to guide fertilization [12]. The long, narrow WE with a bulbous tip was hypothesized to enhance directional ion transport
- Ant Antennae design: Ants detect subtle electric fields with fine, spatially distributed antennae [13]. I mimicked this with narrow, whisker-like WEs to enable spatially localized signal detection
- Platypus Bill design: Platypuses have parallel rows of electroreceptors arranged along their bill to capture temporally varying gradients [14]. I designed this electrode with linear WE segments and a surrounding CE ring to reflect this high-resolution electroreception structure
- Neuronal Dendrite design: Mimicking neurons' high-current-density integration sites, this design includes a central soma-like WE with dendritic projections to emulate localized signal summation [15]
- Ampullae of Lorenzini design: Sharks use these sensory organs to detect voltage gradients in water [16]. This electrode features a circular WE with radiating "canals," a

CE ring, and a nearby RE to replicate their spatial configuration and optimize field detection

Once the concepts were finalized, I began digitizing them into precise CAD models using AutoCAD. This allowed me to enforce strict surface area tolerances ( $\pm 0.5 \text{ mm}^2$ ) using the built-in area calculation tool. Designs that were redundant, difficult to manufacture, or too time-consuming to implement were excluded from this stage. Each CAD model also included a 1 mm margin around the extents of the WE, CE, and RE for insulating layers. The final files were exported in SAT format for import into COMSOL Multiphysics, where I performed the next stage of FEA.

### ***Electrochemistry FEA Simulation Phase***

To simulate the sensor behavior in COMSOL, I employed COMSOL's Secondary Current Distribution (SCD) module, which captures activation overpotentials while simplifying species transport by assuming uniform electrolyte concentration [17]. The relation between charge transfer and overpotential can be described using the Butler–Volmer equation (Equations 3-4) [18]. Ohm's law is used in combination with a charge balance to describe the conduction of currents in the electrodes and electrolytes (Equations 5-6).

$$i_{ct} = i_0 \left( \exp\left(\frac{(1 - \beta)F\eta}{RT}\right) - \exp\left(\frac{-\beta F\eta}{RT}\right) \right) \quad (3)$$

$$\eta = \phi_s - \phi_l - E_0 \quad (4)$$

$$i = -\sigma \nabla \phi \quad (5)$$

$$\nabla \cdot (-\sigma \nabla \phi) = 0 \quad (6)$$

To simplify the simulation, the following assumptions were made:

- The CE is an ideal sink and is sufficiently large and electrically conductive to facilitate current flow from the WE

- The RE is an ideal ground reference and there is negligible current flow
- The electrolyte has constant chemical properties with no gradients (1x PBS with pH 7.4)
- The concentration of H<sub>2</sub>O<sub>2</sub> was set to 10 mM to maximize the magnitudes of the metrics compared between designs and more easily show differences
- There is perfect contact between material interfaces
- The simulation was solved for a steady-state solution with no fluid flow

First, the SAT file for each respective design was imported into COMSOL and the various boundaries and domains were defined including the WE carbon surface, WE silver surface, CE carbon surface, CE silver surface, RE silver surface, total carbon surface, total silver surface, and total current flow surface boundaries, and the electrolyte, WE, and CE domains (Figure 22). Only the surfaces in contact with the electrolyte were included in the boundaries to make the simulation realistic. All other surfaces were modeled as insulated from the electrolyte since in reality they will either be covered by the substrate underneath or by the insulating SEBS material on the top and lateral surfaces. The insulating SEBS layer was modeled as having a 1 mm margin window from the extents of the WE, CE, and RE sensing regions, covering all traces up to the connector pads that would be used to connect the alligator clips.

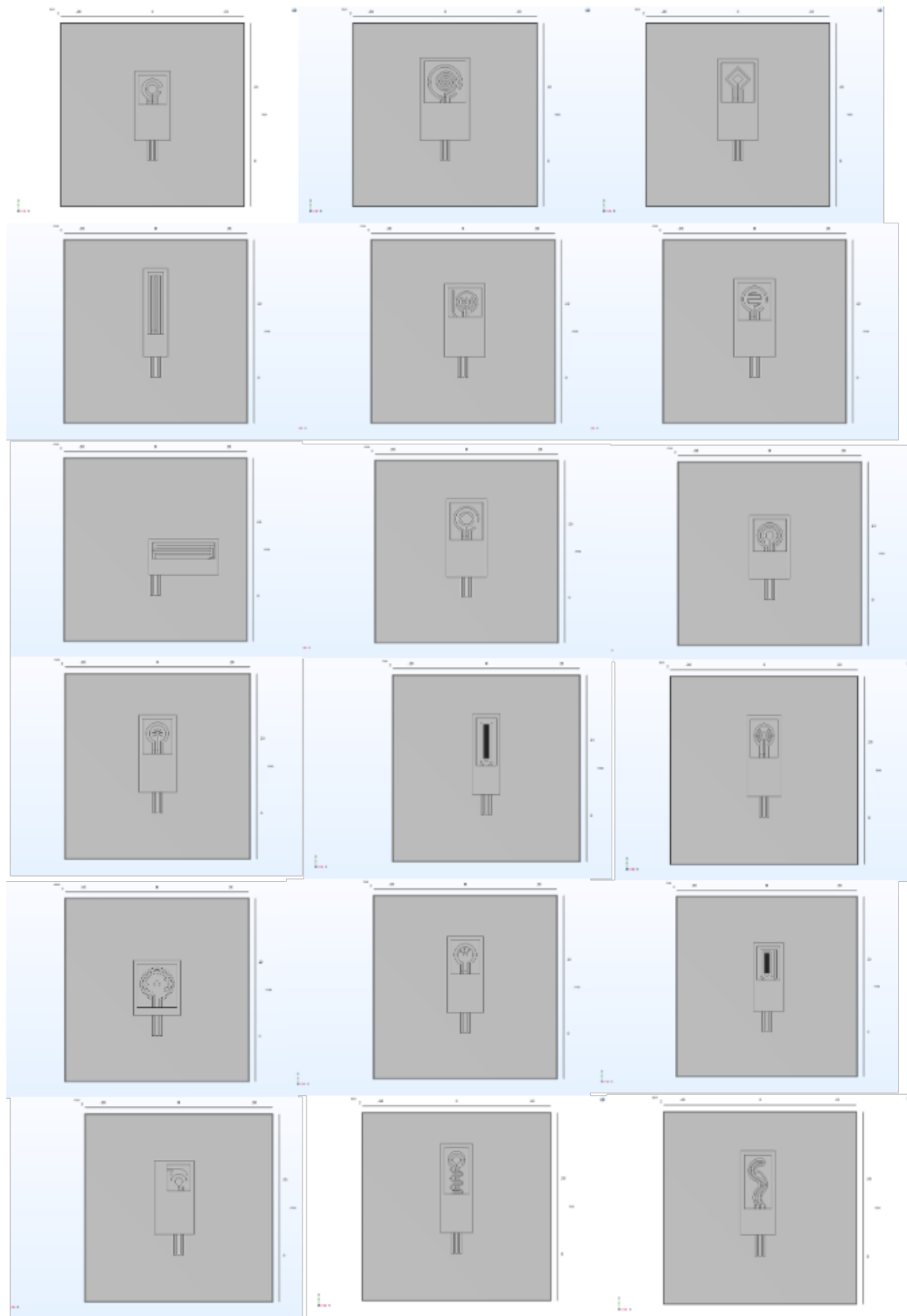
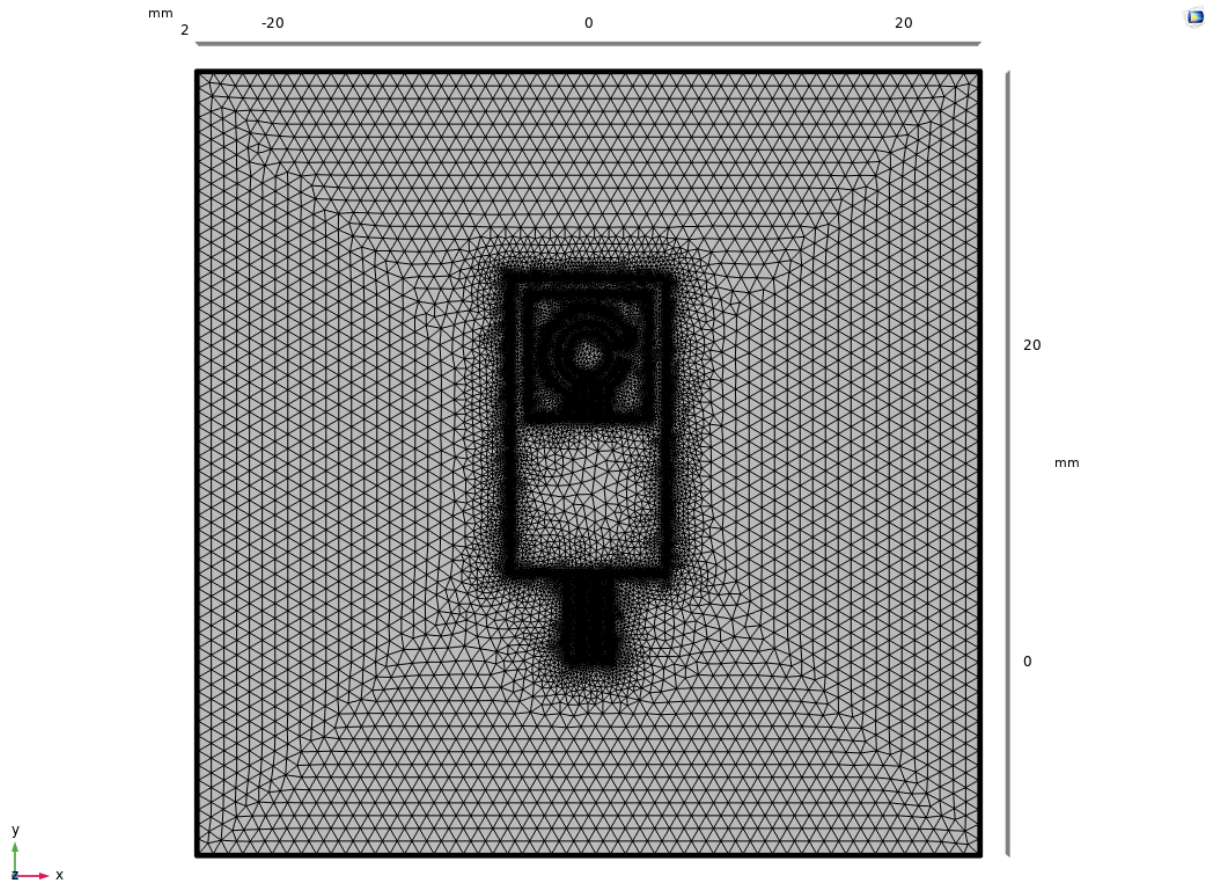


Figure 22. Imported SAT file CAD geometries for COMSOL simulation for 18 different designs.

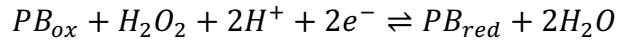
Meshes were created for each geometry using the “Extra Fine” mesh refinement setting in COMSOL, with the exception of the Leaf Drop design which was only able to create a mesh with a “Coarse” refinement due to its geometric complexity causing meshing errors at higher refinement levels (Figure 23). The number of elements averaged around 500,000 for each design.



*Figure 23.* Extra fine mesh for Classic electrode design in COMSOL.

The SCD interface was set up with linear discretization for both the electrolyte potential and the electric potential, and the initial values for both potentials were set to 0 V. The domain for the electrolyte solution was set to a size of  $50 \times 50 \times 3$  mm<sup>3</sup> (assumed to vastly exceed the size of the sensing surfaces of the electrodes) and the electrolyte conductivity of the PBS was set to 1.5 S/m [19]. Electrode surfaces were defined for the WE, CE, and RE boundaries. To more realistically model the electrochemical behavior of the working and counter electrodes, Butler–

Volmer kinetics were incorporated into the COMSOL simulation to represent the PB catalytic layer deposited on the carbon electrode surfaces. PB is well known as an “artificial peroxidase” that efficiently catalyzes the reduction of hydrogen peroxide ( $H_2O_2$ ) at low overpotentials. The surface reaction modeled is:



In this mechanism, PB acts as a redox mediator where  $PB_{ox}$  (PB) is reduced to  $PB_{red}$  (Prussian White/PW) by accepting electrons from the electrode. The local current density at the electrode–electrolyte interface was expressed using the Butler-Volmer equation (Equation 3), where the exchange current density  $i_0$  was defined using Equation 7 [20]:

$$i_0 = nFk'\Gamma_{PW}[H_2O_2] \quad (7)$$

Where  $n$  is the number of electrons transferred,  $F$  is the Faraday constant,  $k'$  is the heterogeneous rate constant for the PB– $H_2O_2$  reaction,  $\Gamma_{PW}$  is the surface concentration of electroactive PB sites, and  $[H_2O_2]$  is the local hydrogen peroxide concentration in the electrolyte

This formulation links the electrocatalytic activity directly to the local peroxide concentration, ensuring that current generation is driven by both the electrode kinetics and mass transport of  $H_2O_2$ . By doing so, the model more accurately predicts the spatial distribution of current density, potential, and power dissipation during chronoamperometric sensing. For further simplification, the anodic and cathodic transfer coefficients were both set to  $\alpha_a = \alpha_c = 0.5$ . The equilibrium potential for all reactions was set to 0 V, and the applied potential at the WE was set to +10 mV in reference to the RE potential. Since there are no reactions at the electrode surface of the RE,  $i_0$  was set to 0 A/m<sup>2</sup>. The electrode surfaces were modeled accurately with separate exchange current density values for the silver (9.65 A/m<sup>2</sup>) and carbon (0.337 A/m<sup>2</sup>) ink boundaries, and only the carbon boundaries were used for electrode reactions [21, 22, 23].

The results collected from the simulation include qualitative plots for electrolyte potential, electrolyte current density, and power dissipation to view symmetry of the potential field, verify current flow from the WE to the CE, and identify locations of high power dissipation concentration (Figure 24). Further quantitative results useful for head-to-head comparison of the designs were total current flow at the WE surface (A), total power loss of all electrode surfaces (W), maximum power dissipation density ( $\text{W}/\text{m}^3$ ), and efficiency which was calculated as the ratio of total current flow at the WE to the total power loss of the sensor (A/W). The power dissipation density was computed using Equation 8 [24]. Furthermore, I developed a novel algorithm to compute a metric I termed the “symmetry score”, which provides a quantitative score for evaluating how symmetric the current distribution is on the WE surface.

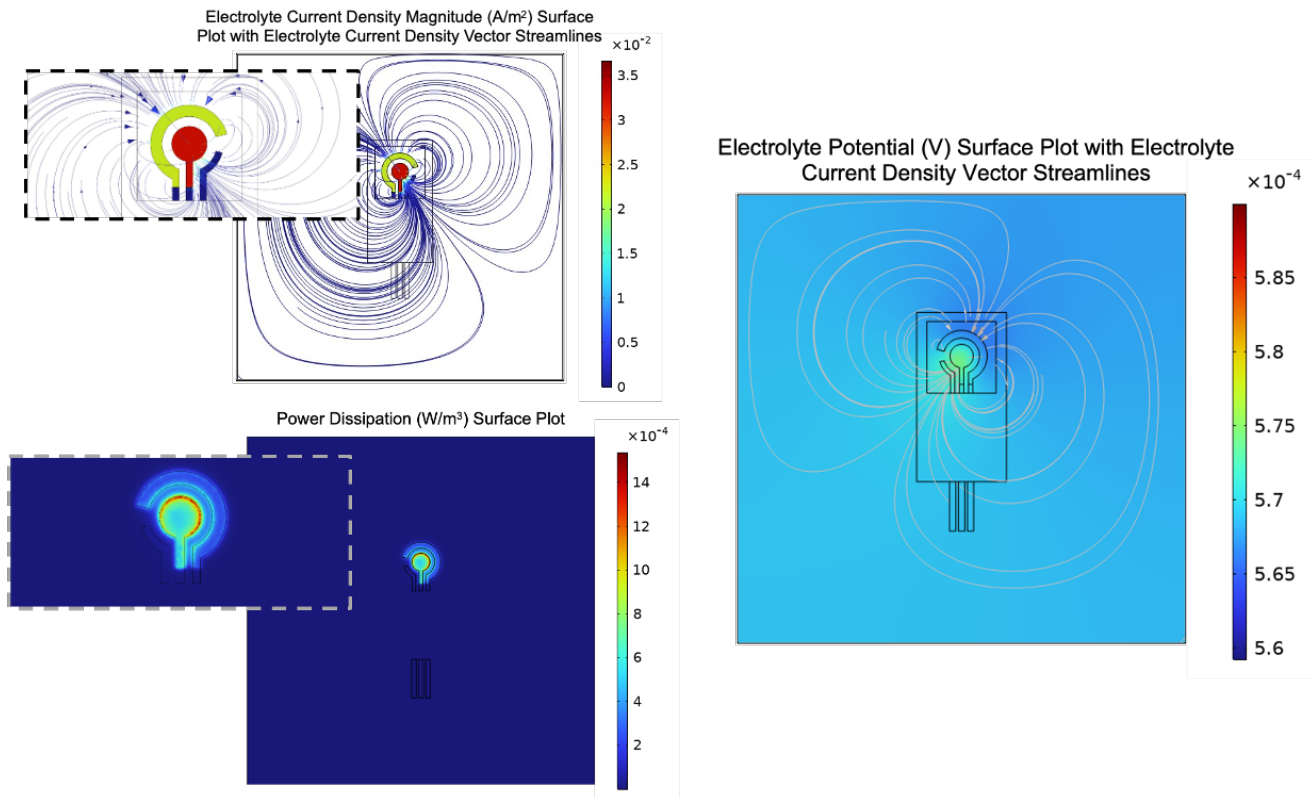


Figure 24. Qualitative COMSOL plots for Classic electrode design.

$$P = \sigma \cdot \|\nabla\phi^2\| = \sigma \cdot (\phi_x^2 + \phi_y^2 + \phi_z^2) \quad (8)$$

To compute the symmetry score, first the COMSOL data was exported as a CSV file and read into a Python notebook as a Pandas data frame including mesh point information for the WE in x-, y-, and z-coordinates and the boundary flux data for those mesh points ( $\text{A/m}^2$ ). Next, the following optimization problem is solved to find the best axis of symmetry for the particular geometry of a given electrode design:

Decision Variable:  $\theta$

Objective: minimize  $\zeta(\theta)$  such that

Bounds:  $0 \leq \theta \leq \pi$  radians

Where  $\zeta(\theta)$  is the symmetry score as a function of an angle offset from the  $y = 0$  axis

The symmetry score function  $\zeta(\theta)$  is calculated by first pinning the axis of symmetry at the centroid of the WE geometry and rotating the axis about the z-axis by an angle of  $\theta$  relative to the  $y = 0$  axis (Figure 25). The centroid of the geometry is found with Equation 9 [25].

$$\text{Centroid } C = (p_x, p_y)$$

$$p_x = \frac{\int x dA}{\int dA}; p_y = \frac{\int y dA}{\int dA} \quad (9)$$

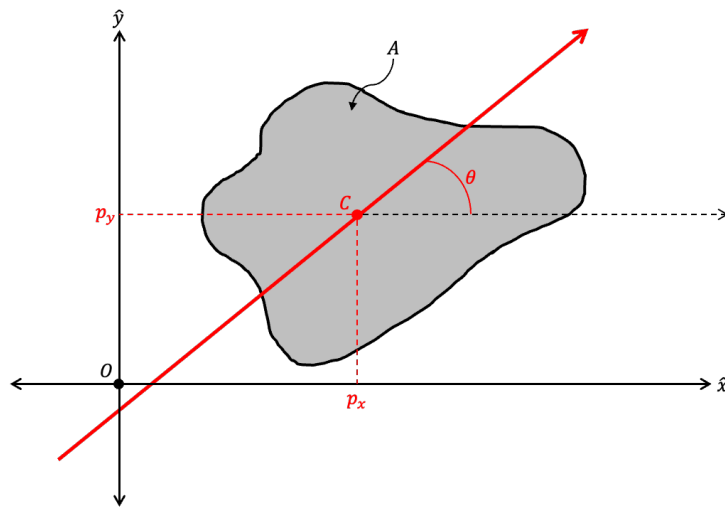


Figure 25. Arbitrary geometry with centroid-pinned axis of symmetry offset by angle  $\theta$ .

The axis of symmetry is modeled as a line rotating about the WE centroid, defined parametrically as a linear function of  $\theta$  in Equation 10 [26]. The symmetry score is calculated by finding the total current via integrating the boundary flux on either side of the axis of symmetry over the area on that half of the geometry and finding the absolute value of the difference of the currents on either side of the axis of symmetry using Equation 11. The score is then normalized to a range between 0 and 1 based on the total current present on the entire surface of the WE (Equation 12). With this normalization the worst-case scenario would be a score of 1 where all the current is on one side of the symmetry axis and the best-case scenario would be a score of 0 where the current on one side of the symmetry axis perfectly matches the current on the opposite side.

$$y - y_1 = m(x - x_1) \therefore y - p_y = \tan \theta (x - p_x) \rightarrow y = x \tan \theta - p_x \tan \theta + p_y$$

$$y = x \tan \theta - \frac{\int x dA}{\int dA} \tan \theta + \frac{\int y dA}{\int dA} \quad (10)$$

$$\forall (p_x, p_y) \in P:$$

$$\text{if } p_y > p_x \tan \theta - \frac{\int x dA}{\int dA} \tan \theta + \frac{\int y dA}{\int dA}$$

$$J(p_x, p_y) \in J^+$$

$$\text{else if } p_y < p_x \tan \theta - \frac{\int x dA}{\int dA} \tan \theta + \frac{\int y dA}{\int dA}$$

$$J(p_x, p_y) \in J^-$$

$$\zeta(\theta) = \left| \sum \int_{A+} J^+ dA - \sum \int_{A-} J^- dA \right| \quad (11)$$

$$\bar{\zeta}(\theta) = \frac{\zeta(\theta)}{\sum \int_{A+} J^+ dA + \sum \int_{A-} J^- dA} \mid 0 \leq \bar{\zeta}(\theta) \leq 1 \quad (12)$$

This simulation procedure was repeated for each of the 18 electrode design geometries and the results were tabulated for head-to-head comparison (Table 1 and Figure 26). The top 5 novel designs with the best combination of efficiency and symmetry scores were selected to advance to the bench-top experiment phase along with the Classic design as a baseline control.

*Table 1.* Simulation results for all 18 electrode design geometries sorted by percent efficiency relative to the Classic design.

Design	Max Power Dissipation (W/m <sup>3</sup> )	Total Energy Loss (W)	Total Current (A)	Symmetry Score	Efficiency (A/W)	Efficiency Improvement from Classic (%)
Serpentine Fingers	816.85	4.19E-12	2.81E-7	0.001760	67086.22	86.00%
Simple	303.90	5.13E-12	3.26E-7	0.000345	63538.19	76.16%
Shield	412.93	5.08E-12	3.16E-7	0.000192	62225.89	72.52%
Serpentine Dot	4157.11	5.77E-12	3.15E-7	0.000506	54551.13	51.24%
Leaf Drop	271.10	5.05E-12	2.56E-7	0.011105	50603.72	40.30%
Neuronal Dendrite	897.99	5.24E-12	2.57E-7	0.000038	49003.88	35.86%
Zig Zag	547.30	6.56E-12	3.11E-7	0.000050	47438.46	31.52%
Ring	590.61	6.94E-12	3.28E-7	0.000034	47335.56	31.24%
Ampullae of Lorenzini	645.16	5.59E-12	2.53E-7	0.000089	45219.60	25.37%
Ant Antennae	518.78	7.19E-12	3.23E-7	0.000223	44985.53	24.72%
Trident	604.83	7.28E-12	3.27E-7	0.000070	44924.89	24.55%
Platypus Bill	648.72	8.13E-12	3.65E-7	0.000048	44915.95	24.53%
L-Interdigitated	3874.04	7.33E-12	3.26E-7	0.000620	44449.30	23.24%
Diamond	410.55	6.86E-12	2.98E-7	0.000145	43397.11	23.32%
Mormyrid Fish Electroreceptor	311.25	5.43E-12	2.11E-7	0.000220	38934.22	7.95%
Classic	463.25	7.90E-12	2.85E-7	0.004633	36068.44	-
Pollen Tube	557.12	5.89E-12	1.87E-7	0.003189	31683.30	-12.16%
Curly	2198.10	2.04E-12	6.30E-7	0.000027	30902.75	-14.32%

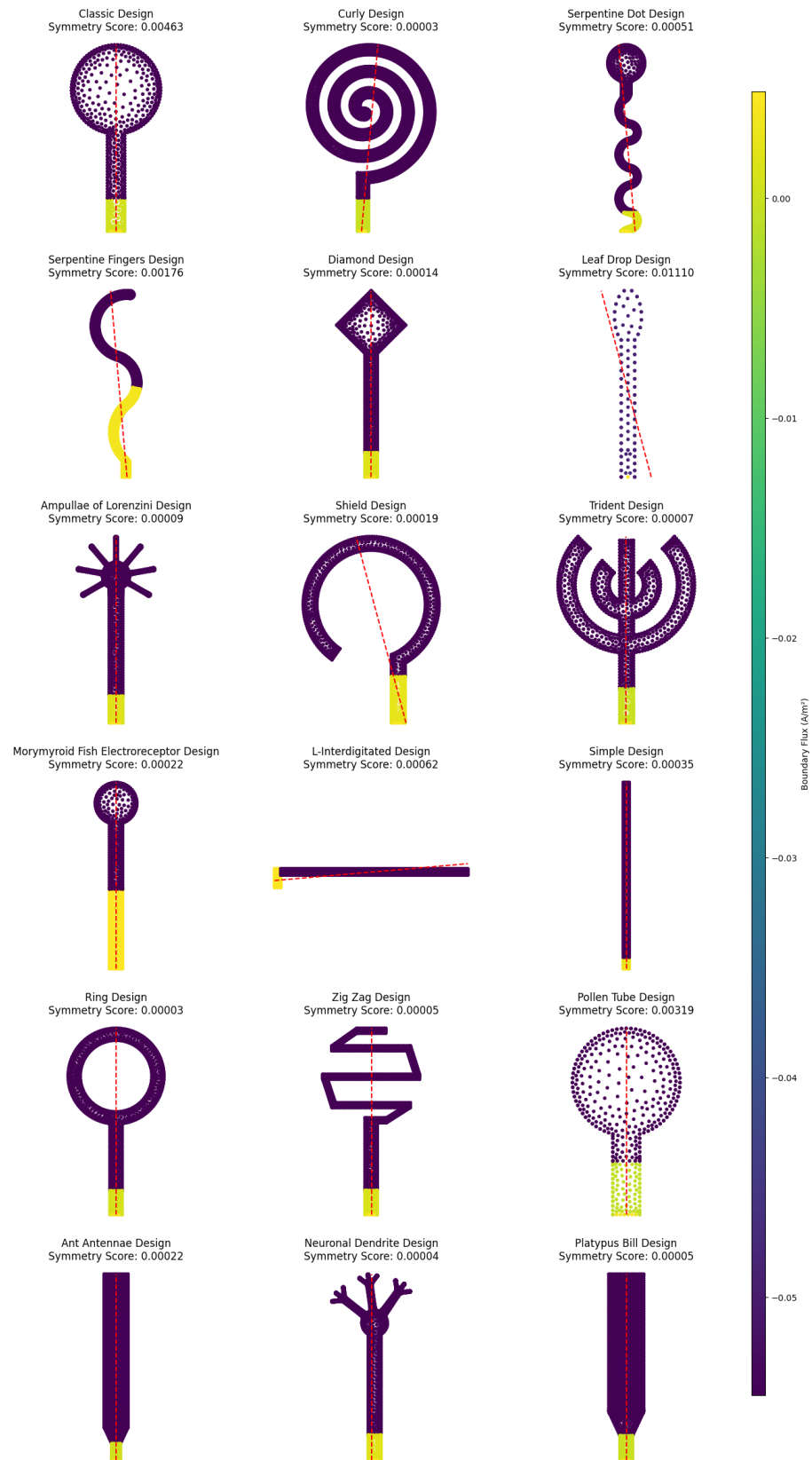


Figure 26. Symmetry scores along with optimal symmetry axis calculated for each electrode design.

The five designs selected for experimental fabrication — Serpentine Fingers, Serpentine Dot, Leaf Drop, Neuronal Dendrite, and Ampullae of Lorenzini — were chosen based on general trends observed in their electrical efficiency and symmetry performance. Rather than applying strict thresholds, the selection was guided by designs that demonstrated strong tradeoffs between maximizing current output per unit power loss (A/W) and maintaining geometric symmetry, which was hypothesized to support signal stability and uniformity in real-world performance. Each design brought unique advantages. Serpentine Fingers offered the highest efficiency overall (+86% improvement over the classical design), making it the leading candidate despite its relatively poor symmetry score. Serpentine Dot provided strong efficiency and symmetry balance, suggesting it can offer both high sensitivity and stability. Leaf Drop was the most geometrically complex design and served as a useful upper bound for manufacturability while still maintaining excellent performance. Neuronal Dendrite had the second best symmetry score among all designs and maintained high efficiency, making it a biologically inspired option with robust electrochemical balance. Ampullae of Lorenzini, also bioinspired, exhibited strong symmetry and respectable efficiency, making it a well-rounded, stable candidate.

These top five designs were originally selected based on simulation results prior to the inclusion of electrode reaction kinetics. At the time, my simulation modeled only PBS electrolyte and assumed perfect electrochemical behavior at the electrodes, neglecting the specific redox reaction of PB with H<sub>2</sub>O<sub>2</sub>. These original results were used to guide the initial fabrication batch prior to my travel to visit family. While preparing this final report, I gained a stronger understanding of the underlying mathematics governing the simulation and the simulation was significantly improved to include Butler-Volmer reaction kinetics at the PB-modified electrodes, accounting for the catalytic behavior of PB toward H<sub>2</sub>O<sub>2</sub> reduction. The updated model yields a

more physically accurate spatial distribution of current and Joule heating, enabling more faithful prediction of real-world sensor performance. Despite this improvement, the original top 5 designs remained among the highest performers, validating the earlier selections. However, two designs — Simple and Shield — exhibited notably better performance in the improved model and may merit inclusion in future experiments. These can be incorporated into subsequent trials during the semester to assess whether the simulated gains translate into experimental performance improvements.

### ***Electrode Fabrication Phase***

Having narrowed down the top designs based on the simulation results I then exported each AutoCAD drawing as a DXF file and imported them into Inkscape to convert to two separate PNG files with a dots per inch (DPI) of 1270 – one for the silver/silver-chloride print layers and another for the carbon print layers. This DPI is the setting that the lab uses for the Dimatix inkjet printer to have a  $20\text{ }\mu\text{m}$  ink drop spacing. The PNG files were then imported into GIMP to convert the images to 1-bit monochrome BMP files, and this is the file format that is used for the printer.

With the files ready, I proceeded to fabricate the electrodes using the Dimatix DMP-2800 inkjet printer. This printer is a highly specialized and sensitive machine, and operating it is significantly more involved than simply uploading a file and pressing “print” like a 3D printer. It requires expert knowledge of jetting parameters, cleaning procedures, ink preparation, and substrate handling. In fact, very few users globally are proficient in its full operation, and in the lab, only the graduate students were trained to use it properly. There was no formal written protocol provided, so I took the initiative to carefully document every step I learned from

Katherine, a PhD student in the lab, and created a comprehensive, step-by-step inkjet printing protocol to guide the process.

The printing process began with preparation of the 3-mil Kapton polyimide substrate, which is especially prone to contamination due to its electrostatic nature. Cleanliness is essential to achieve consistent ink spreading, prevent defects, and ensure proper layer adhesion. The cleaning process involved first taping the substrate to the lab bench and using Scotch tape to lift dust and debris from both sides. This was followed by wiping each side with isopropanol (IPA) in circular motions three times using Kim wipes. The substrate was then taped vertically to a clean shelf, sprayed with IPA, and allowed to air dry. A compressed air source was used to speed up the drying process. Once dry, the substrate was carefully aligned on the print bed, with the smooth side facing up and vacuum holes around the perimeter dotted with a Sharpie for later realignment. A small “X” was also marked at the origin point for precise reference when reloading the substrate during the second ink printing phase.

Next, I prepared the silver nanoparticle ink (Metalon JS-B25HV) by either using a refrigerated cartridge or preparing a new one using a syringe, needle, and the appropriate filter. After filtering and filling the cartridge, the ink was allowed to sit upright to stabilize, per manufacturer recommendations. The cartridge was then installed into the printer along with a fresh cleaning pad, and the Drop Watcher tool was used to identify well-functioning jets. A small set of adjacent jets was selected to ensure clean, even deposition.

The BMP image of the silver pattern was imported into the printer software, and the DPI was specified (1270 dpi, or 20  $\mu\text{m}$  drop spacing), and exported as a PTF file for printing. Before printing, the head angle and origin were calibrated using the fiducial camera. Silver traces were printed in up to 3 layers, checking after each layer to ensure sufficient coverage. Once complete,

the substrate was removed and baked at 250°C for 20 minutes to sinter the silver nanoparticles and reduce resistance.

After silver printing, the carbon ink (Metalon JR-700LV) was prepared and loaded using the same protocol. The silver ink cartridge and cleaning pad were removed and replaced with those for carbon. Using the previously marked alignment dots and origin, the carbon pattern was loaded and printed directly flush with the silver regions. Carbon was printed in two stages of 4 layers each, with a 2-hour bake at 250°C following each stage to ensure full curing without cracking or delamination. This 8-layer stack was chosen based on preliminary tests that Katherine had conducted that showed a significant drop in resistance with increased carbon thickness.

Finally, the last step was cleaning up by turning the vacuum off, cleaning and refrigerating the ink cartridges, wiping the print bed clean with IPA, and returning all materials to the appropriate storage. The full fabrication workflow is outlined in detail in the protocol document I created.

With the substrate aligned, I began the printing process. Initially, I aimed to complete the full printing workflow before leaving for my trip to Jordan, so I attempted the first run independently without Katherine's supervision. Unfortunately, the first print (Figure 27) resulted in poor quality: the silver ink was over-deposited and pooled into uneven blobs, creating large globs that shorted the connector pads.

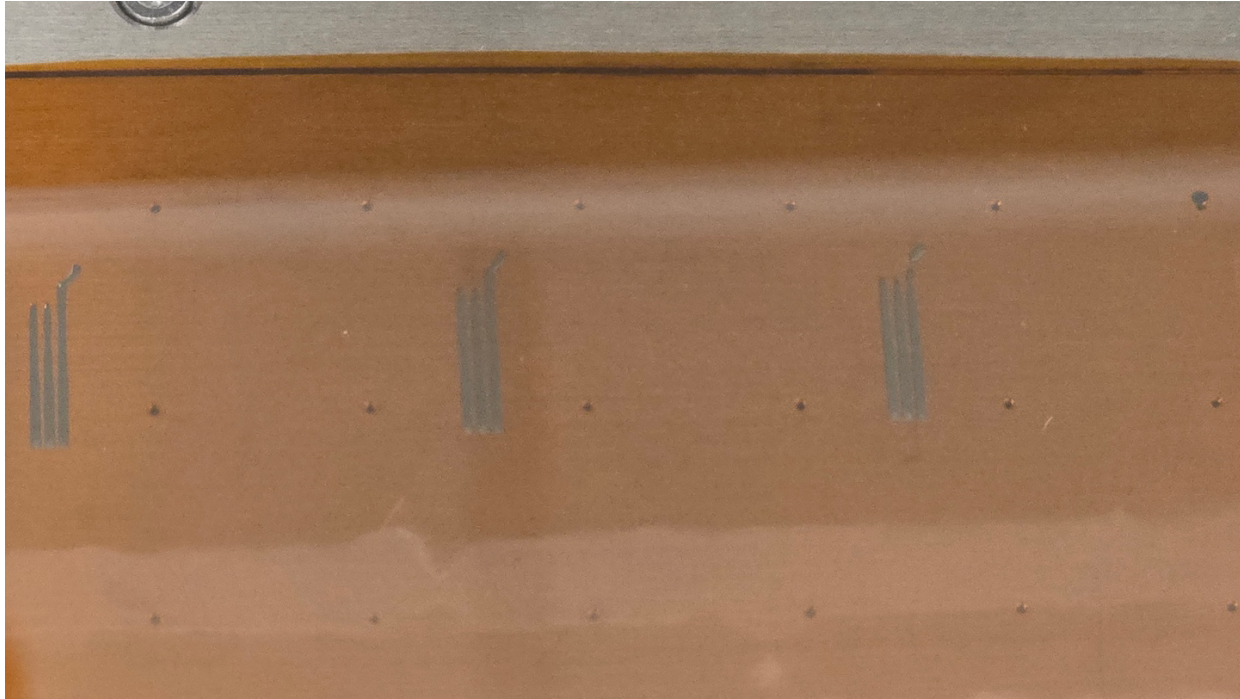


*Figure 27.* First attempted silver ink print with blobs causing traces to come out thicker and shorting each other.

I traced these failures to several avoidable issues:

1. I mistakenly used 1-mil Kapton instead of the specified 3-mil, resulting in substrate warping and poor vacuum adherence
2. The DPI of the BMP file was set too high for the printer to handle, which overloaded the jetting resolution
3. I incorrectly removed the vacuum hole masking tape from the bed, reducing the vacuum pressure needed to hold the substrate flat
4. The YouTube Dimatix tutorial cleaning method I had followed was inadequate [27]. I later learned a superior method from Katherine that eliminated dust and oils more effectively
5. The connector pad design I used was incompatible with the FPC connector due to the substrate's thinness, so I redesigned it to use 4x4 mm square pads for direct alligator clip attachment

In the second attempt (Figure 28 and Figure 29), I implemented these corrections and printed with the modified connector geometry. However, I noticed a different failure mode: the silver ink was not fully covering the intended pattern and produced incomplete, spotty prints. Upon inspection, I discovered that the JS-B25HV silver ink I was using was expired, potentially leading to clogging or inconsistent droplet formation. I found a non-expired silver ink cartridge (Metalon JS-A101A) and switched to it after the first layer. Initially, the fill looked promising, but after baking using the parameters recommended for JS-B25HV (250°C for 20 minutes), the ink layer cracked severely, rendering the sensors unusable. This indicated that the A101A ink has different thermal curing requirements.

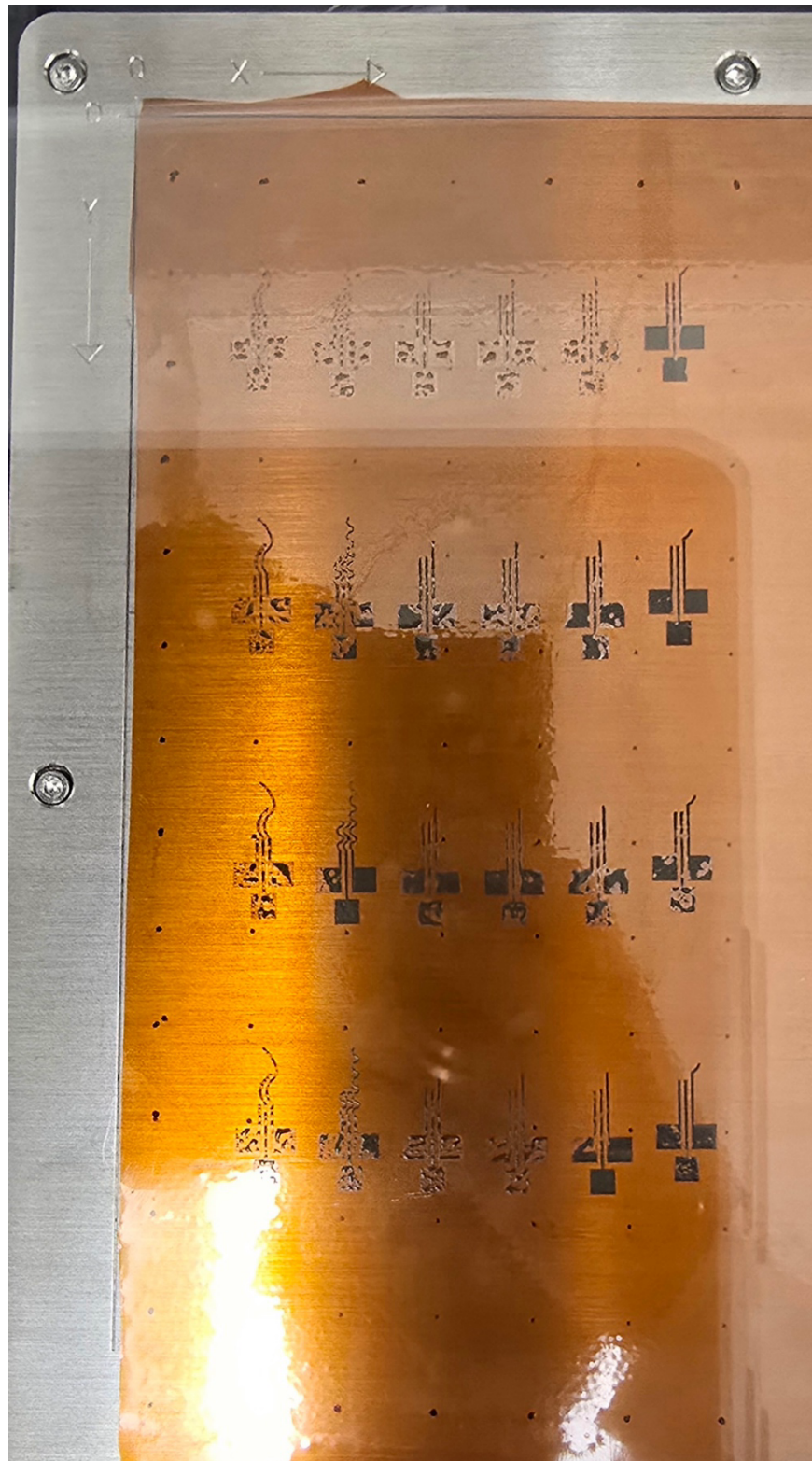


Figure 28. Second attempt at printing silver ink layer. Sparse jetting resulted in splotchy and fragmented traces and connector pads with the JS-B25HV ink.

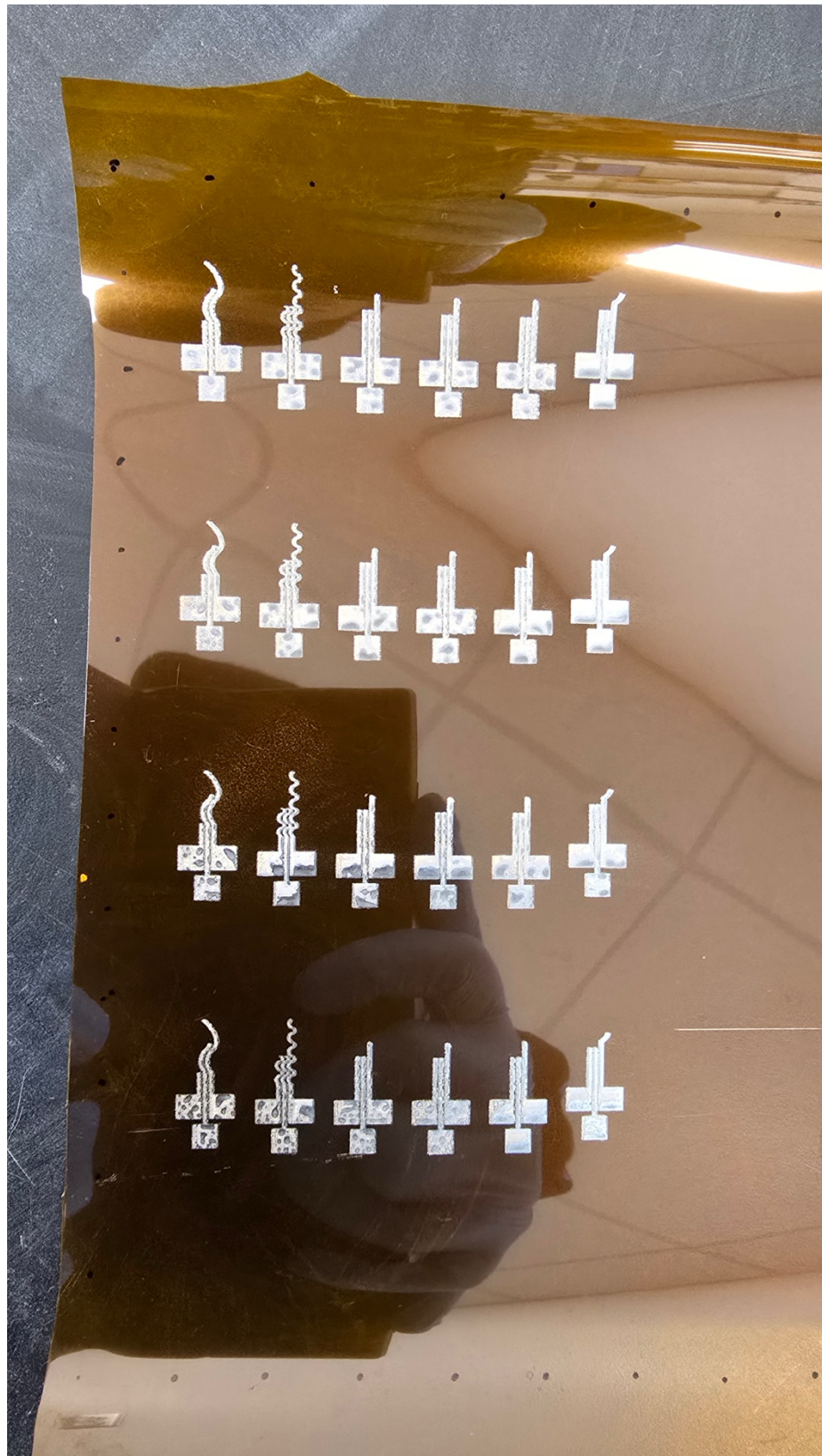


Figure 29. Second attempt at printing silver ink layer. Switching to JS-A101A ink mid-print and baking using same procedure as JS-B25HV ink resulted in significant cracking and fuzziness at edges causing shorting.

For the third and final attempt before I left (Figure 30 and Figure 31), I returned to using the JS-B25HV ink and dramatically shortened the cleaning interval between prints to avoid nozzle clogging. This adjustment significantly improved the print quality. Although not perfect, the final silver layer was complete enough for testing purposes. Post-baking inspection showed no cracking or delamination. Rather than immediately printing the carbon layer over the finished silver layer, I tested the carbon ink printing on a small, unused section of the substrate to verify alignment and quality. The test was successful, so I proceeded to print the first four layers of the carbon ink, followed by a 2-hour bake at 250°C. On my final day in the lab, I attempted to print the remaining four layers of carbon but encountered a major issue: no ink was jetting during Drop Watcher inspection, and even attempting to print directly yielded no output. After multiple cartridge swaps and extensive debugging, I identified two main problems: the piezoelectric tab on one of the cartridges was defective causing the printer to crash, and I had mistakenly left the Drop Watcher firing frequency at the default 5 kHz when carbon ink requires 36 kHz to jet properly. Once I corrected the setting and refilled the original cartridge, the carbon ink began jetting again. The second carbon print aligned well with the silver layer, and I completed the final four-layer print and baked it for 2 hours. Resistance measurements across the carbon working electrode paths yielded values around 8 kΩ, which is comparable to the 6 kΩ achieved by Katherine in her optimal prints suggesting these sensors are within the expected functional range.

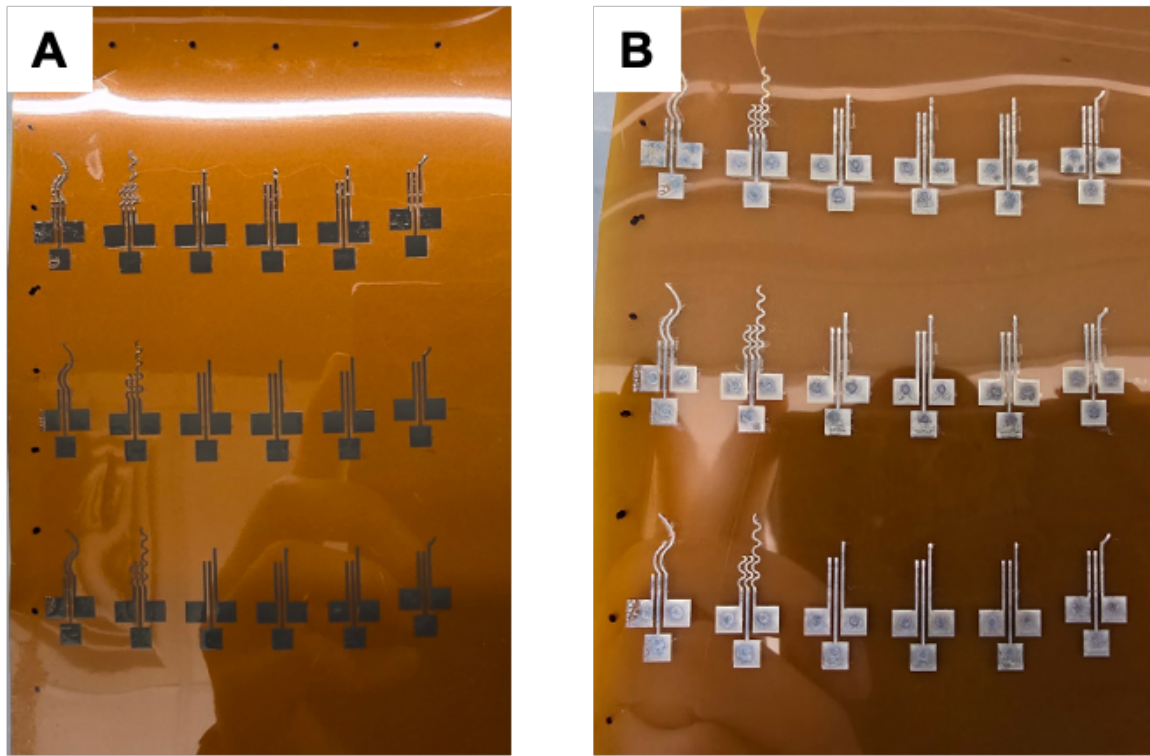


Figure 30. Third attempt at printing silver layer A) before and B) after baking.

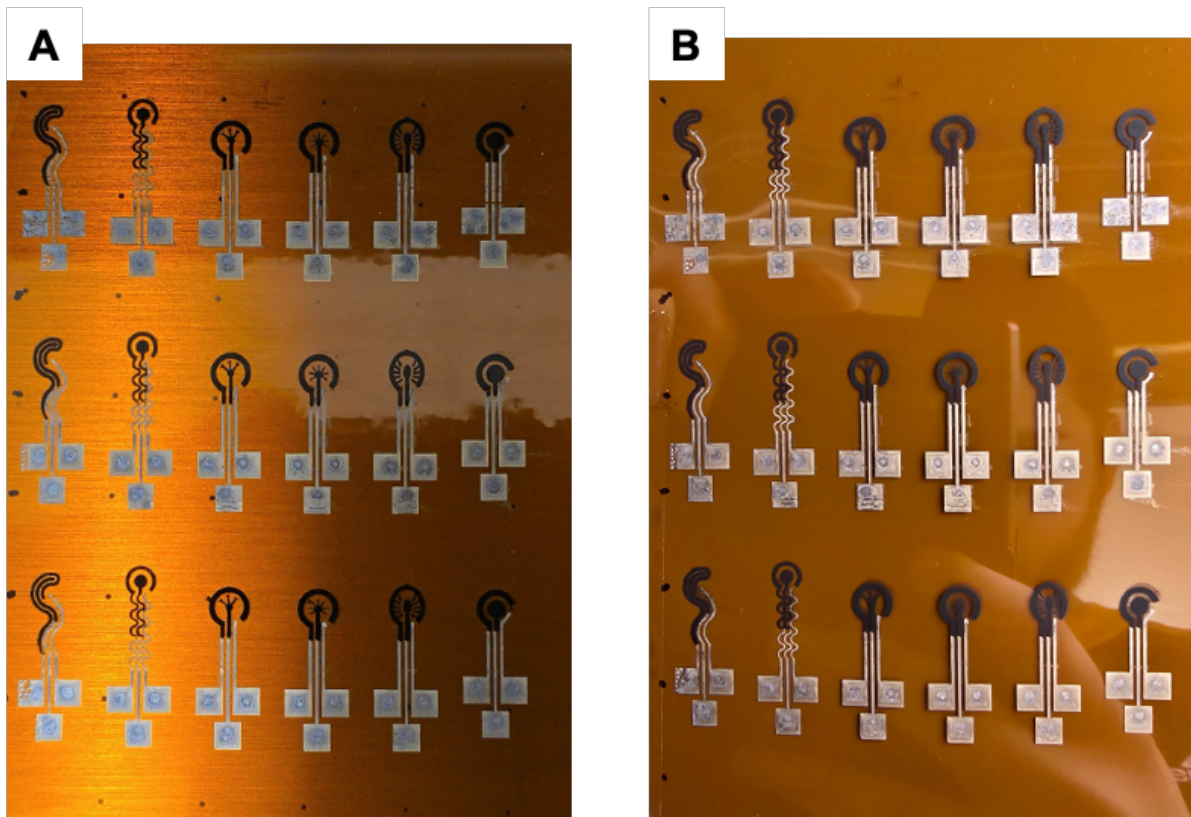


Figure 31. Third attempt at fabricating sensors with silver and carbon printed layers A) before and B) after baking.

In summary, despite a steep learning curve and tight time constraints, I was able to fabricate my first batch of biosensors with both silver and carbon layers correctly deposited. While additional refinements are planned, the successful deposition of both layers and acceptable resistance measurements ( $\sim 8 \text{ k}\Omega$ ) confirm this batch is suitable for initiating electrochemical characterization. This outcome validates the feasibility of the workflow and lays the groundwork for systematic testing and potential replication with improved consistency. I am considering printing a second, cleaner batch now that I fully understand the workflow and common pitfalls, but testing the current sensors is also a viable next step.

### ***Electrode Study Next Steps***

With the initial simulations and fabrication complete, there are several clear next steps required to strengthen and complete the electrode design study. These steps will refine the design constraints, improve experimental validation, and enable robust statistical comparison across geometries.

In the original simulations, a simplified constraint system was used: total planar surface areas of carbon and silver ink were fixed across all designs, without differentiating how much of each was allocated to the WE, CE, or RE, nor were trace lengths or pad geometries standardized. However, Dr. Sempionatto raised an important point – variations in CE-to-WE ratios, WE surface area, or trace geometries may confound the comparison between designs. To address this, the next design iteration will implement stricter constraints:

- Fixed WE carbon, WE silver, CE carbon, CE silver, and RE silver planar surface areas for all designs
- Equalized trace lengths to standardize ohmic contributions
- Standardized connector pad sizes

This will isolate electrode shape as the sole independent variable, ensuring a more rigorous and fair head-to-head evaluation of electrode performance.

To further improve the validity of the simulation phase, I will also conduct a mesh refinement study in COMSOL. This study will evaluate the sensitivity of the simulation output to mesh element size across a representative subset of the electrode geometries (such as one conventional, one low-efficiency, and one top-performing bio-inspired design). I will record the calculated metrics including total current and total power loss across progressively finer mesh refinements (including “Normal,” “Fine,” “Extra Fine”) and monitor convergence behavior. This process will ensure that the chosen mesh density yields stable, accurate results without unnecessary computational overhead and will strengthen the credibility of the simulation-based screening pipeline.

The updated electrode geometries will be printed using the Dimatix DMP-2800 inkjet printer. Now that the full fabrication pipeline has been mastered and a working protocol developed, the second batch of sensors will have improved alignment, reduced resistance, and more consistent print quality. The new connector geometries will be retained to support direct alligator clip testing. Following silver and carbon printing, the sensors will be chemically modified with PB to enable H<sub>2</sub>O<sub>2</sub> electrocatalysis. This can be done by drop-casting a PB solution on the WE and allowing it to dry under ambient conditions, following established protocols used in biosensor literature [28].

Each design will be tested for H<sub>2</sub>O<sub>2</sub> detection using a CHI potentiostat. The experiment involves using alligator clips to connect to the sensor pads and taping the cables to the bench to prevent motion artifacts. The concentration range of the H<sub>2</sub>O<sub>2</sub> will range from 0 to ~300 μM, which was chosen to align with common test ranges used in R&D settings, with 20 μM steps for

21 total measurements [29]. To prepare the appropriate concentrations, a dilution protocol will be followed that splits it into two dilution steps:

1. 5.1  $\mu\text{L}$  of stock 30% w/w  $\text{H}_2\text{O}_2$  (9.8M) into 4995  $\mu\text{L}$  MilliQ water  $\rightarrow \sim 10 \text{ mM H}_2\text{O}_2$
2. 102  $\mu\text{L}$  of 10 mM intermediate dilution into 898  $\mu\text{L}$  MilliQ  $\rightarrow 1020 \mu\text{M H}_2\text{O}_2$

I will start with pipetting 100  $\mu\text{L}$  of 1x PBS at a pH of 7.4 on the sensor, then sequentially add 2  $\mu\text{L}$  of 1020  $\mu\text{M H}_2\text{O}_2$  stock at each step to reach the target concentrations (Table 2).

*Table 2.* H<sub>2</sub>O<sub>2</sub> concentration preparation protocol.

Step	H <sub>2</sub> O <sub>2</sub> Added (μL)	Final Volume (μL)	Target [H <sub>2</sub> O <sub>2</sub> ] (μM)
0	0	100	0.00
1	2	102	20.00
2	4	104	39.23
3	6	106	57.74
4	8	108	75.56
5	10	110	92.73
6	12	112	109.29
7	14	114	125.26
8	16	116	140.69
9	18	118	155.59
10	20	120	170.00
11	22	122	183.93
12	24	124	197.42
13	26	126	210.48
14	28	128	223.13
15	30	130	235.38
16	32	132	247.27
17	34	134	258.81
18	36	136	270.00
19	38	138	280.87
20	40	140	291.43
21	42	142	301.69

For each sensor, the experiment will begin with a CV scan in pure PBS to determine the redox peak voltages, particularly the cathodic peak associated with PB reduction. This voltage will be used as the potential for subsequent chronoamperometry measurements. CA will be used as the primary analytical technique and will be conducted by holding the potential at the chosen value and waiting for the current to stabilize typically within 20 minutes before adding each aliquot of H<sub>2</sub>O<sub>2</sub>. This process will be repeated for all 21 concentration increments. The resulting current readings will then be used to generate calibration curves of current versus H<sub>2</sub>O<sub>2</sub> concentration for each electrode design.

The data from the CV scans will be analyzed using several performance metrics: anodic and cathodic peak currents, anodic and cathodic peak potentials, absolute current at the switching potential, background noise current, and peak-to-peak voltage separation [30]. These will help reveal electron transfer kinetics and reversibility of the PB-modified electrodes [31]. For CA, key metrics will include steady-state Faradaic current magnitude, capacitive current behavior, time to reach stabilization at each step, and overall current profile. From the current vs. concentration calibration curves, the sensitivity of each sensor will be calculated as the slope of the linear regression fit, and linearity will be assessed using the coefficient of determination ( $r^2$ ) [32]. Repeatability will be determined as the standard deviation of current at each concentration across the three replicate sensors for each design [33]. Signal-to-noise ratio (SNR) will be computed as the ratio between the mean current at each non-zero  $\text{H}_2\text{O}_2$  concentration and the standard deviation of the baseline signal in PBS before  $\text{H}_2\text{O}_2$  is added [34]. The linear range and limit of detection (LOD) will be estimated using the IUPAC convention, typically defined as the concentration interval over which the response is linear within 5% deviation, or alternatively calculated as  $\frac{3.3 \times \sigma_{blank}}{\text{slope}}$ , where  $\sigma_{blank}$  is the standard deviation of the blank response [35]. If time permits, sensor longevity will also be evaluated by repeating the full measurement protocol at 24-hour intervals over three days and monitoring the decline in sensitivity, allowing extrapolation of the device lifetime based on when the signal degrades to 50% of the original slope [36].

Finally, for statistical analysis of the electrode performance across different geometries, one-way ANOVA will be conducted independently for each metric mentioned above, with post-hoc comparisons performed using Tukey's HSD test to determine statistically significant pairwise differences between designs. A one-way ANOVA with Tukey's post-hoc test is

appropriate for identifying statistically significant performance differences between electrode designs, assuming homogeneity of variance and independent replicates. This approach will help identify whether observed improvements in efficiency, sensitivity, or stability are statistically meaningful, and will inform selection of lead candidates for further optimization.

### Concluding Remarks and Future Outlook

This summer was an incredibly transformative experience that allowed me to take ownership of two ambitious and technically challenging projects: custom electrochemical electrode design and PCB development for integrated biosensing. Both projects pushed me to think critically across multiple engineering domains, combining insights from electrical engineering, chemistry, software, mathematics, and materials science to solve real-world biosensing challenges.

For the electrode design study, I went from initial hand-drawn sketches to fully simulated designs in COMSOL, developing a computational framework to assess electrical efficiency and symmetry across novel geometries. I devised a pipeline that included algorithmic evaluation in Python, printed the first batch of sensors using a highly complex inkjet printing system, and prepared the groundwork for benchtop H<sub>2</sub>O<sub>2</sub> testing. Through this process, I developed advanced CAD and simulation expertise, learned how to operate one of the world's most sophisticated fabrication tools, and built a deep intuition about the design constraints and trade-offs in electrochemical sensing systems. More importantly, I now have a clear path forward: refining the designs with tighter constraints to isolate geometry effects, testing performance with PB-modified electrodes, and analyzing results with rigorous statistical and analytical tools. The consistency between my initial and updated simulation results gives me confidence in the methodology, and with the foundational work already done, this study is well-positioned to become a publication during the Fall semester.

In parallel, the PCB development project exposed me to end-to-end hardware system design. I designed a custom board with electrochemical front-ends, power regulation, and microcontroller integration, and I now plan to revise and improve the board with new insights

gained from my work on DialySafe. This includes upgrading the power circuitry, improving layout robustness with stitching vias and test points, and developing firmware using EVAL kits ahead of full hardware integration. This project gives me a powerful platform to characterize both commercial and custom-designed sensors in a flexible, modular way, and lays the foundation for future on-body sensing platforms.

Collectively, these projects reflect a diverse and powerful engineering skill set that spans simulation, hardware design, firmware development, rapid prototyping, and scientific experimentation. I learned how to design power-efficient circuits, fabricate high-resolution electrodes, troubleshoot electrochemical instrumentation, and structure experimental protocols with statistical rigor which are the kinds of cross-disciplinary skills that industry R&D teams look for whether in medical devices, wearables, biotechnology, or advanced manufacturing.

More broadly, these contributions have real potential to help shape the future direction of the Sempionatto Lab at Rice University. This is Dr. Sempionatto's first year at Rice, and being able to contribute to the lab's foundational research and infrastructure has been a privilege. These early-stage studies (both the custom sensor geometries and the portable electrochemical measurement system) can serve as springboards for future graduate and undergraduate research. I'm excited to continue working in the lab throughout the coming semester to build on this momentum and bring these projects to their full potential.

In short, this summer has not only advanced my technical and analytical skills but has also solidified my confidence and passion for solving complex, interdisciplinary problems. Whether in academia or industry, I now feel more prepared than ever to take on engineering challenges that require systems thinking, creativity, and resilience.

## References

- [1] S. M. Naghib, S. M. Katebi and S. Ghorbanzade, *Electrochemical Biosensors in Practice: Material and Methods*, Tehran: Bentham Books, 2023.
- [2] A. U. Sardesai, V. N. Dhamu, A. Paul, S. Muthukumar and S. Prasad, "Design and Electrochemical Characterization of Spiral Electrochemical Notification Coupled Electrode (SENCE) Platform for Biosensing Application," *Micromachines*, vol. 11, no. 3, p. 333, 2020.
- [3] G. L. Goh, M. F. Tay, J. M. Lee, J. S. Ho, L. N. Sim, W. Y. Yeong and T. H. Chong, "Potential of Printed Electrodes for Electrochemical Impedance Spectroscopy (EIS): Toward Membrane Fouling Detection," *Advanced Electronic Materials*, vol. 7, 2021.
- [4] J. Min, S. Demchyshyn, J. R. Sempionatto, Y. Song, B. Hailegnaw, C. Xu, Y. Yang, S. Solomon, C. Putz, L. E. Lehner, J. F. Schwarz, C. Schwarzinger, M. C. Scharber and E. S. Sani, "An Autonomous Wearable Biosensor Powered by a Perovskite Solar Cell," *Nature Electronics*, vol. 6, pp. 630-641, 2023.
- [5] F. Tehrani, H. Teymourian, B. Wuerstle, J. Kavner, R. Patel, A. Furmidge, R. Aghavali, H. Hosseini-Toudeshki, C. Brown, F. Zhang, K. Mahato, Z. Li, A. Barfidokht, L. Yin and P. Warren, "An Integrated Wearable Microneedle Array for the Continuous Monitoring of Multiple Biomarkers in Interstitial Fluid," *Nature Biomedical Engineering*, vol. 6, pp. 1214-1224, 2022.

- [6] J. Fan, Q. Du, Z. Dong, J. Zhao and T. Xu, "Design of the Jump Mechanism for a Biomimetic Robotic Frog," *Biomimetics*, vol. 7, no. 4, p. 142, 2022.
- [7] F. Shahid, M. Alam, J.-Y. Park, Y. Choi, C.-J. Park, H.-K. Park and C.-Y. Yi, "Bioinspired Morphing in Aerodynamics and Hydrodynamics: Engineering Innovations for Aerospace and Renewable Energy," *Biomimetics*, vol. 10, no. 7, p. 427, 2025.
- [8] H. M. K. K. M. B. Herath, N. Madusanka, S. L. P. Yasakethu, C. Hewage and B.-I. Lee, "Biomimetic Robotics and Sensing for Healthcare Applications and Rehabilitation: A Systematic Review," *Biomimetics*, vol. 10, no. 7, p. 466, 2025.
- [9] N. P. Hyun, J. P. Olberding, A. De, S. Divi, X. Liang, E. Thomas, R. St. Pierre, E. Steinhardt, J. Jorge, S. J. Longo, S. Cox, E. Mendoza, G. P. Sutton, E. Azizi, A. J. Crosby, S. Bergbreiter, R. J. Wood and S. N. Patek, "Spring and Latch Dynamics Can Act as Control Pathways in Ultrafast Systems," *Bionispiration & Biomimetics*, vol. 18, 2023.
- [10] G. Sakurai and J. S. Miklavcic, "On the Efficacy of Water Transport in Leaves. A Coupled Xylem-Phloem Model of Water and Solute Transport," *Frontiers in Plant Science*, vol. 12, 2021.
- [11] P. Moller, "Electroreception and the Behaviour of Mormyrid Electric Fish," *Trends in Neuroscience*, vol. 3, no. 5, pp. 105-109, 1980.
- [12] C. Agudelo, M. Packirisamy and A. Geitmann, "Influence of Electric Fields and Conductivity on Pollen Tube Growth Assessed via Electrical Lab-On-Chip," *Scientific Reports*, vol. 6, 2016.

- [13] C. Jiang, H. Xu, L. Yang, J. Liu, Y. Li, K. Takei and W. Xu, "Neuromorphic Antennal Sensory System," *Nature Communications*, vol. 15, 2024.
- [14] J. E. Gregory, A. Iggo, A. K. McIntyre and U. Proske, "Electroreceptors in the Platypus," *Nature*, vol. 326, pp. 386-387, 1987.
- [15] S. Wang, X. Wang and M. A. Holland, "Multi-Physics Modeling and Finite Element Formulation of Neuronal Dendrite Growth with Electrical Polarization," *Brain Multiphysics*, vol. 4, 2023.
- [16] M. H. Hofmann, "Detection and Generation of Electric Signals | Physiology of Ampullary Electrosensory Systems," in *Encyclopedia of Fish Physiology*, Bonn, Academic Press, 2011, pp. 359-365.
- [17] COMSOL Multiphysics, "The Primary Current Distribution and Secondary Current Distribution Interfaces," [Online]. Available: [https://doc.comsol.com/5.6/doc/com.comsol.help.battery/battery\\_ug\\_electrochem.07.003.html](https://doc.comsol.com/5.6/doc/com.comsol.help.battery/battery_ug_electrochem.07.003.html). [Accessed 9 August 2025].
- [18] T. F. Fuller and J. N. Harb, "Electrochemical Kinetics," in *Electrochemical Engineering*, Hoboken, John Wiley & Sons, 2018, pp. 41-59.
- [19] C. V. Chaparro, L. V. Herrera, A. M. Melendez and D. A. Miranda, "Considerations on electrical impedance measurements of electrolyte solutions in a four-electrode cell," *Journal of Physics: Conference Series*, vol. 687, no. 1, 2016.
- [20] J. Kieninger, *Electrochemical Methods for Biosensors, MEMS, Nanotechnology, Neuroscience, Renewable Energy, Batteries* 2nd Edition, Freiburg: De Gruyter, 2025.

- [21] N. N. S. B. M. Musa and A. S. Tijani, "Effect of exchange current density and charge transfer coefficient on performance characteristics of voltage of alkaline electrolysis," *Applied Energy*, vol. 394, 2025.
- [22] H. Ha and J. Payer, "The Effect of Silver Chloride Formation on the Kinetics of Silver Dissolution in Chloride Solution," *Electrochimica Acta*, vol. 56, no. 7, pp. 2781-2791, 2011.
- [23] E. P. Randviir, "A cross examination of electron transfer rate constants for carbon screen-printed electrodes using Electrochemical Impedance Spectroscopy and cyclic voltammetry," *Electrochimica Acta*, vol. 286, pp. 179-186, 2018.
- [24] S. W. Ellingson, "Power Dissipation in Conducting Media," in *Electromagnetics I*, Blacksburg, VT Publishing, 2018.
- [25] R. C. Hibbeler, "Center of Gravity and Centroid," in *Engineering Mechanics: Statics and Dynamics 14th Edition*, Hoboken, Pearson Prentice Hall, 2016, pp. 465-476.
- [26] I. Al-Akash, "The Ultimate All-In-One Compendium to Learn Linear Algebra: Part 1," Texas Institute of Technology Innovation and Science, 23 December 2023.  
[Online]. Available: <https://texitis.com/linalg/>. [Accessed 9 August 2025].
- [27] L. Rizzo, "Dimatix Printer," YouTube, 20 August 2020. [Online]. Available:  
<https://www.youtube.com/playlist?list=PLosugf0bSu4T2UfEMEzYipnReH9RBV4qf>. [Accessed 2 August 2025].
- [28] F. Ricci, A. Amine, C. S. Tuta, A. A. Ciucu, F. Lucarelli, G. Palleschi and D. Moscone, "Prussian Blue and enzyme bulk-modified screen-printed electrodes for hydrogen

- peroxide and glucose determination with improved storage and operational stability," *Analytica Chimica Acta*, vol. 485, no. 1, pp. 111-120, 2003.
- [29] A. O. Tjell, B. Jud, R. Schaller-Ammann and T. Mayr, "Optical hydrogen peroxide sensor for measurements in flow," *Sensors and Actuators B: Chemical*, vol. 400, no. Part B, 2024.
- [30] M. Rafiee, D. J. Abrams, Z. Goss, A. Romero-Arenas and S. S. Stahl, "Cyclic Voltammetry and Chronoamperometry: Mechanistic Tools for Organic Electrosynthesis," *Chemical Society Reviews*, vol. 53, no. 2, pp. 566-585, 2024.
- [31] C. Sandford, M. A. Edwards, K. J. Klunder, D. P. Hickey, L. Min, K. Barman, M. S. Sigman, H. S. White and S. D. Minteer, "A synthetic chemist's guide to electroanalytical tools for studying reaction mechanisms," *Chemical Science*, vol. 10, pp. 6404-6422, 2019.
- [32] K. Toth, K. Stulik, W. Kutner, Z. Feher and E. Lindner, " 7171 total citations on Dimensions. Cite this Cite this Electrochemical detection in liquid flow analytical techniques: Characterization and classification (IUPAC Technical Report)," *Pure Applied Chemistry*, vol. 76, no. 6, pp. 1119-1138, 2004.
- [33] M. Raninec, "Overcoming the Technical Challenges of Electrochemical Gas Sensing," *Analog Devices Technical Articles*, 2019.
- [34] T. Xu, L. Yang, X. Zhang, G. Lu and Z. Bai, "A highly sensitive electrochemical sensor by growing Ag nanoparticles on the surface of PPy@PEDOT:PSS film for detecting sodium hydroxymethanesulfinate molecules," *Food Chemistry: X*, vol. 18, 2023.

- [35] G. L. Long and J. D. Winefordner, "Limit of detection. A closer look at the IUPAC definition," *Analytical Chemistry*, vol. 55, no. 7, 1983.
- [36] Y. Zuo, L. Lei, K. Huang, Q. Hao, C. Zhao and H. Liu, "Improving the in vivo stability and sensor lifetime with new blend membranes on CGM sensors," *RSC Applied Polymers*, no. 5, 2024.